LAWRENCE
LIVERMORE
NATIONAL
LABORATORY

LLNL-JRNL-403219

OGLE-2005-BLG-071Lb, the Most Massive M-Dwarf Planetary Companion?

S. Dong, A. Gould, A. Udalski, J. Anderson, G. W. Christie, B. S. Gaudi, M. Jaroszynski, M. Kubiak, M. K. Szymanski, G. Pietrzynski, I. Soszynski, O. Szewczyk , K. Ulaczyk, L. Wyrzykowski, D. L. DePoy, D. B. Fox, A. Gal-Yam, C. Han, S. Lepine, J. McCormick, E. Ofek, B.-G. Park, R. W. Pogge, F. Abe, D. P. Bennett, I. A. Bond, T. R. Britton, A. C. Gilmore, J. B. Hearnshaw, Y. Itow, K. Kamiya, P. M. Kilmartin, A. Korpela, K. Masuda, Y. Matsubara, M. Motomura, Y. Muraki, S. Nakamura, K. Ohnishi, C. Okada, N. Rattenbury, To. Saito, T. Sako, M. Sasaki, D. Sullivan, T. Sumi, P. J. Tristram, T. Yanagisawa, P. C. M. Yock, T. Yoshoika, M. D. Albrow, J. P. Beaulieu, S. Brillant, H. Calitz, A. Cassan, K. H. Cook, Ch. Coutures, S. Dieters, D. Dominis Prester, et al.

April 25, 2008

Astrophysical Journal

Disclaimer

OGLE-2005-BLG-071Lb, the Most Massive M-Dwarf Planetary Companion?

Subo Dong[1,2], Andrew Gould[1,2], Andrzej Udalski[3,4], Jay Anderson[5], G.W. Christie[1,6], B. S. Gaudi[1,2],
and
M. Jaroszyński[4], M. Kubiak[4], M. K. Szymański[4], G. Pietrzyński[4,7], I. Soszyński[4], O. Szewczyk[7,4], K. Ulaczyk[4], Ł. Wyrzykowski[8,4]
(The OGLE Collaboration),
D. L. DePoy[2], D. B. Fox[9], A. Gal-Yam[10], C. Han[11], S. Lépine[12], J. McCormick[13], E. Ofek[14], B.-G. Park[15], R. W. Pogge[2],
(The μFUN Collaboration),
F. Abe[16], D. P. Bennett[17,18], I. A. Bond[19], T. R. Britton[20], A. C. Gilmore[20].
J. B. Hearnshaw[20], Y. Itow[16], K. Kamiya[16], P. M. Kilmartin[21], A. Korpela[22], K. Masuda[16], Y. Matsubara[16], M. Motomura[16], Y. Muraki[23], S. Nakamura[16], K. Ohnishi[24], C. Okada[16], N. Rattenbury[25], To. Saito[26], T. Sako[16], M. Sasaki[16], D. Sullivan[22], T. Sumi[16], P. J. Tristram[21], T. Yanagisawa[27], P. C. M. Yock[28], T. Yoshoika[16],
(The MOA Collaboration)
M.D. Albrow[20], J.P. Beaulieu[29], S. Brillant[30], H. Calitz[31], A. Cassan[32], K. H. Cook[33], Ch. Coutures[29], S. Dieters[34], D. Dominis Prester[35], J. Donatowicz[36], P. Fouqué[37], J. Greenhill[34], K. Hill[34], M. Hoffman[31], K. Horne[38], U.G. Jørgensen[39], S. Kane[40], D. Kubas[30], J.B. Marquette[29], R. Martin[41], P. Meintjes[31], J. Menzies[42], K.R. Pollard[20], K.C. Sahu[5], C. Vinter[39], J. Wambsganss[32], A. Williams[41], M. Bode[43], D.M. Bramich[44], M. Burgdorf[43], C. Snodgrass[30], I. Steele[43],
(The PLANET/RoboNet Collaborations)
Vanessa Doublier[45], and Cedric Foelmi[46].

[1]Microlensing Follow-Up Network (μFUN).

[2]Department of Astronomy, Ohio State University, 140 W. 18th Ave., Columbus, OH 43210, USA; dong, gaudi, gould, depoy, pogge@astronomy.ohio-state.edu.

[3]Optical Gravitational Lens Experiment (OGLE).

[4]Warsaw University Observatory, Al. Ujazdowskie 4, 00-478 Warszawa, Poland; udalski, mj, msz, mk, pietrzyn, soszynsk, kulaczyk@astrouw.edu.pl.

[5]Space Telescope Science Institute, Baltimore MD; jayander@stsci.edu.

[6]Auckland Observatory, Auckland, New Zealand; gwchristie@christie.org.nz.

[7]Universidad de Concepción, Departamento de Fisica, Casilla 160–C, Concepción, Chile; szewczyk@astro-udec.cl.

[8]Institute of Astronomy, University of Cambridge, Madingley Road, Cambridge CB3 0HA, UK; wyrzykow@ast.cam.ac.uk.

[9]Astronomy & Astrophysics, Pennsylvania State University, 525 Davey Laboratory, University Park, PA 16802; dfox@astro.psu.edu.

[10]Benoziyo Center for Astrophysics, Weizmann Institute of Science, 76100 Rehovot, Israel; avishay.gal-yam@weizmann.ac.il.

[11]Program of Brain Korea, Department of Physics, Chungbuk National University, 410 Seongbong-Rho, Hungduk-Gu, Chongju 371-763, Korea; cheongho@astroph.chungbuk.ac.kr.

[12]Department of Astrophysics, Division of Physical Sciences, American Museum of Natural History, Central Park West at 79th Street, New York, NY 10024, USA; lepine@amnh.org.

[13]Farm Cove Observatory, Centre for Backyard Astrophysics, Pakuranga, Auckland New Zealand; farm-coveobs@xtra.co.nz.

[14]Division of Physics, Mathematics and Astronomy, California Institute of Technology, Pasadena, CA 91125; eran@astro.caltech.edu.

[15]Korea Astronomy and Space Science Institute, 61-1 Hwaam-Dong, Yuseong-Gu, Daejeon 305-348, Korea; bgpark@kasi.re.kr.

[16]Solar-Terrestrial Environment Laboratory, Nagoya University, Nagoya, 464-8601, Japan.

[17]Department of Physics, 225 Nieuwland Science Hall, Notre Dame University, Notre Dame, IN 46556, USA.

[18]Probing Lensing Anomalies NETwork (PLANET) Collaboration.

[19]Institute for Information and Mathematical Sciences, Massey University, Private Bag 102-904, Auckland 1330, New Zealand.

[20]University of Canterbury, Department of Physics and Astronomy, Private Bag 4800, Christchurch 8020, New Zealand.

[21]School of Chemical and Physical Sciences, Victoria University, Wellington, New Zealand.

[22]Mt. John Observatory, P.O. Box 56, Lake Tekapo 8770, New Zealand.

[23]Department of Physics, Konan University, Nishiokamoto 8-9-1, Kobe 658-8501, Japan.

[24]Nagano National College of Technology, Nagano 381-8550, Japan.

[25]Jodrell Bank Centre for Astrophysics, The University of Manchester, Manchester, M13 9PL, UK.

[26]Tokyo Metropolitan College of Industrial Technology, Tokyo 116-8523, Japan.

[27]Advanced Space Technology Research Group, Institute of Aerospace Technology, Japan Aerospace Exploration Agency (JAXA), Tokyo, Japan

[28]Department of Physics, University of Auckland, Private Bag 92-019, Auckland 1001, New Zealand.

[29]Institut d'Astrophysique de Paris, 98bis Boulevard Arago, 75014 Paris, France.

[30]European Southern Observatory, Casilla 19001, Vitacura 19, Santiago, Chile.

[31]Dept. of Physics / Boyden Observatory, University of the Free State, Bloemfontein 9300, South Africa.

[32]Astronomisches Rechen-Institut, Zentrum für Astronomie, Heidelberg University, Mönchhofstr. 12–14, 69120 Heidelberg, Germany

[33]Lawrence Livermore National Laboratory, IGPP, P.O. Box 808, Livermore, CA 94551, USA

[34]University of Tasmania, School of Maths and Physics, Private bag 37, GPO Hobart, Tasmania 7001, Australia

[35]Department of Physics, University of Rijeka, Omladinska 14, 51000 Rijeka, Croatia

[36]Technical University of Vienna, Dept. of Computing, Wiedner Hauptstrasse 10, Vienna, Austria

[37]LATT, Université de Toulouse, CNRS, 14 av. E. Belin, 31400 Toulouse, France

[38]SUPA, University of St Andrews, School of Physics & Astronomy, North Haugh, St Andrews, KY16 9SS, United Kingdom

[39]Niels Bohr Institute, Astronomical Observatory, Juliane Maries Vej 30, DK-2100 Copenhagen, Denmark

[40]Michelson Science Center, California Institute of Technology, MS 100-22, 770 South Wilson Avenue, Pasadena, CA 91125, USA

[41]Perth Observatory, Walnut Road, Bickley, Perth 6076, Australia

[42]South African Astronomical Observatory, P.O. Box 9 Observatory 7935, South Africa

[43]Astrophysics Research Institute, Liverpool John Moores University, Twelve Quays House, Egerton Wharf, Birkenhead CH41 1LD, UK

[44]Isaac Newton Group of Telescopes, Apartado de Correos 321, E-38700 Santa Cruz de la Palma, Canary Islands, Spain

[45]ESO, Karl-Schwarzschild-Strasse 2, D-85748 Garching bei Mnchen

[46]LAOG, Observatoire de Grenoble BP 53 F-38041 GRENOBLE, France

ABSTRACT

We combine all available information to constrain the nature of OGLE-2005-BLG-071Lb, the second planet discovered by microlensing and the first in a high-magnification event. These include photometric and astrometric measurements from *Hubble Space Telescope*, as well as constraints from higher-order effects extracted from the ground-based light curve, such as microlens parallax, planetary orbital motion and finite-source effects. Our primary analysis leads to the conclusion that the host of Jovian planet OGLE-2005-BLG-071Lb is a foreground M dwarf, with mass $M = 0.46 \pm 0.04\,M_\odot$, distance $D_l = 3.3 \pm 0.4\,\mathrm{kpc}$, and thick-disk kinematics $v_{\rm LSR} \sim 103\,\mathrm{km\,s^{-1}}$. From the best-fit model, the planet has mass $M_p = 3.5 \pm 0.3\,M_{\rm Jupiter}$, lies at a projected separation $r_\perp = 3.6 \pm 0.2\,\mathrm{AU}$ from its host and has an equilibrium temperature of $T \sim 50$ K, i.e., similar to Neptune. A degenerate model less favored by $\Delta\chi^2 \sim 4$ gives essentially the same planetary mass $M_p = 3.3 \pm 0.3\,M_{\rm Jupiter}$ with a smaller projected separation, $r_\perp = 2.1 \pm 0.1\,\mathrm{AU}$, and higher equilibrium temperature $T \sim 68$ K. These results from the primary analysis suggest that OGLE-2005-BLG-071Lb is likely to be the most massive planet yet discovered that is hosted by an M dwarf. However, the formation of such high-mass planetary companions in the outer regions of M-dwarf planetary systems is predicted to be unlikely within the core-accretion scenario. There are a number of caveats to this analysis, but these could mostly be resolved by a single astrometric measurement a few years after the event.

Subject headings: gravitational lensing – planetary systems – Galaxy: bulge

1. Introduction

Microlensing provides a powerful method to detect extrasolar planets. Although only six microlens planets have been found to date (Bond et al. 2004; Udalski et al. 2005; Beaulieu et al. 2006; Gould et al. 2006; Gaudi et al. 2008), these include two major discoveries. First, two of the planets are "cold Neptunes", a high discovery rate in this previously inaccessible region of parameter space, suggesting this new class of extrasolar planets is common (Gould et al. 2006; Kubas et al. 2008). Second, the discovery of the first Jupiter/Saturn analog via a very high magnification event with substantial sensitivity to multiple planets indicates that Solar System analogs may be prevalent among planetary systems (Gaudi et al. 2008). Recent improvements in search techniques and future major upgrades should increase the discovery rate of microlensing planets substantially (Gaudi 2007).

Routine analysis of planetary microlensing light curves yields the planet/star mass ratio q and the planet-star projected separation b (in units of the angular Einstein radius). However, because the lens-star mass M cannot be simply extracted from the light curve, the planet mass $M_p = qM$ remains, in general, equally uncertain.

The problem of constraining the lens mass M is an old one. When microlensing experiments were initiated in the early 1990s, it was generally assumed that individual mass measurements would be impossible and that only statistical estimates of the lens mass scale could be recovered. However, Gould (1992) pointed out that the mass and lens-source relative parallax $\pi_{\rm rel}$ are simply related to two observable parameters, the angular Einstein radius $\theta_{\rm E}$ and the projected Einstein radius $\tilde{r}_{\rm E}$,

$$M = \frac{\theta_{\rm E}}{\kappa \pi_{\rm E}}, \qquad \pi_{\rm rel} = \theta_{\rm E} \pi_{\rm E}. \tag{1}$$

Here, $\pi_{\rm E} = {\rm AU}/\tilde{r}_{\rm E}$ is the "microlens parallax" and $\kappa \equiv 4G/(c^2\,{\rm AU}) \sim 8.1\,{\rm mas}/M_\odot$. In principle, $\theta_{\rm E}$ can be measured by comparing some structure in the light curve to a "standard angular ruler" on the sky. The best example is light-curve distortions due to the finite angular radius of the source θ_* (Gould 1994), which usually can be estimated quite well from its color and apparent magnitude (Yoo et al. 2004). While such finite-source effects are rare for microlensing events considered as a whole, they are quite common for planetary events. The reason is simply that the planetary distortions of the light curve are typically of similar or smaller scale than θ_*. In fact, all six planetary events discovered to date show such effects. Combining $\theta_{\rm E}$ with the (routinely measurable) Einstein radius crossing time $t_{\rm E}$ yields the relative proper motion μ in the geocentric frame,

$$\mu_{\rm geo} = \frac{\theta_{\rm E}}{t_{\rm E}}, \tag{2}$$

From equation (1), measurement of $\theta_{\rm E}$ by itself fixes the product $M\pi_{\rm rel} = \theta_{\rm E}^2/\kappa$. Using priors on the distribution of lens-source relative parallaxes, one can then make a statistical estimate of the lens mass M and so the planet mass M_p.

To do better, one must develop an additional constraint. This could be measurement of the microlens parallax $\pi_{\rm E}$, but this is typically possible only for long events. Another possibility is direct detection of the lens, either under the "glare" of the source during and immediately after the event, or displaced from the source well after the event is over. Bennett et al. (2006) used the latter technique to constrain the mass of the first microlensing planet, OGLE-2003-BLG-235/MOA-2003-BLG-53Lb. They obtained *Hubble Space Telescope (HST)* Advanced Camera for Surveys (ACS) images in B, V, and I at an epoch $\Delta t = 1.78$ years after the event. They found astrometric offsets of the (still overlapping) lens and source light

among these images of up to 0.7 mas. Knowing the lens-source angular separation $\Delta\theta = \mu\Delta t$ from the already determined values of $\theta_{\rm E}$ and $t_{\rm E}$, they were able to use these centroid offsets to fix the color and magnitude of the lens and so (assuming it was a main-sequence star) its mass.

While the planet mass is usually considered to be the most important parameter that is not routinely derivable from the light curve, the same degeneracy impacts two other quantities as well, the distance and the transverse velocity of the lens. Knowledge of these quantities could help constrain the nature of the lens, i.e., whether it belongs to bulge, the foreground disk, or possibly the thick disk or even the stellar halo. Since microlensing is the only method currently capable of detecting planets in populations well beyond the solar neighborhood, extracting such information would be quite useful. Because the mass, distance, and transverse velocity are all affected by a common degeneracy, constraints on one quantity are simultaneously constraints on the others. As mentioned above, simultaneous measurements of $\theta_{\rm E}$ and $\pi_{\rm E}$ directly yield the mass. However, clearly from equation (1) they also yield the distance, and hence (from eq. [2]) also the transverse velocity. Here, we assemble all available data to constrain the mass, distance and transverse velocity of the second microlensing planet, OGLE-2005-BLG-071Lb, whose discovery we previously reported (Udalski et al. 2005, hereafter Paper I).

2. Overview of Data and Types of Constraints

The light curve consists of 1398 data points from 9 ground-based observatories (see Fig. 1), plus two epochs of *HST* ACS data in the F814W (I) and F555W (V) filters. The primary ground-based addition relative to Paper I is late-time data from OGLE, who continued to monitor the event down to baseline until HJD = 2453790.9.

These data potentially provide constraints on several parameters in addition to those reported in Paper I. First, the light curve shows a clear asymmetry between the rising and falling part of the light curve, which is a natural result of microlens parallax due to the Earth's accelerated motion around the Sun (see the best-fit model without parallax effects plotted in dotted line in Fig. 1). However, it is important to keep in mind that such distortions are equally-well produced by "xallarap" due to accelerated motion of the source around a companion. Poindexter et al. (2005) showed that it can be difficult to distinguish between the two when, as in the present case, the effect is only weakly detected.

Second, the two pronounced peaks of the light curve, which are due to "cusp approaches" (see the bottom inset of Fig. 1), are relatively sharp and have good coverage. These peaks

would tend to be "rounded out" by finite-source effects, so in principle it may be possible to measure ρ (that is, θ_* in the units of $\theta_{\rm E}$) from these distortions.

Third, orbital motion of the planet can give rise to two effects: rotation of the caustic about the center of the mass and distortion of the caustic due to expansion/contraction of the planet-star axis. The first changes the orientation of the caustic structure as the event evolves while the second changes its shape. These effects are expected to be quite subtle because the orbital period is expected to be of order 10 years while the source probes the caustic structure for only about 4 days. Nevertheless, they can be quite important for the interpretation of the event.

Finally, the *HST* data cover two epochs, one at 23 May 2005 (indicated by the arrow in Fig. 1) when the magnification was about $A = 2$ and the other at 21 Feb 2006 when the event was very nearly at baseline, $A \sim 1$. These data could potentially yield four types of information. First, they can effectively determine whether the blended light is "associated" with the event or not. If this light is due to the lens, a companion to the lens, or a companion to the source, it should fall well within the ACS point spread function (PSF) of the source. On the other hand, if it is due to a random interloper along the line of sight, then it should be separately resolved by ACS or at least give rise to a distorted PSF. Second, the *HST* data can greatly improve the estimate of the color of the blended light. The original model determined the source fluxes in both OGLE V and I quite well, and of course the baseline fluxes are also quite well determined. So it would seem that the blended fluxes, which are the differences between these two, would also be well determined. This proves to be the case in I band. However, while the source flux is derivable solely from flux differences over the light curve (and so is quite well determined from OGLE difference image analysis – DIA – Wozniak 2000), the baseline flux depends critically on the zero point of PSF-fitting photometry, whose accuracy is fundamentally limited in very crowded bulge fields. The small zero-point errors turn out to have no practical impact for the relatively bright I background light, but are important for V band. Third, one might hope to measure a centroid shift between the two colors in the manner of Bennett et al. (2006). Last, one can derive the source proper motion $\boldsymbol{\mu}_s$ from *HST* data (at least relative to the mean motion of bulge stars). This is important, because the event itself yields the source-lens *relative* proper motion, $\boldsymbol{\mu}_{\rm geo}$. Hence, precise determination of $\boldsymbol{\mu}_l$ requires knowledge of two proper-motion differences, first the heliocentric proper motion

$$\boldsymbol{\mu}_{\rm hel} = \boldsymbol{\mu}_l - \boldsymbol{\mu}_s, \tag{3}$$

and second, the offset between the heliocentric and geocentric proper motions

$$\boldsymbol{\mu}_{\rm hel} - \boldsymbol{\mu}_{\rm geo} = \frac{\boldsymbol{v}_\oplus \pi_{\rm rel}}{\rm AU}. \tag{4}$$

Here, $\boldsymbol{v}_\oplus$ is the velocity of the Earth relative to the Sun at the time of peak magnification

t_0. Note that, if the lens-source relative parallax $\pi_{\rm rel}$ is known, even approximately, then the latter difference can be determined quite well.

3. Constraining the Physical Properties of the Lens and its Planetary Companion

In principle, all the effects summarized in § 2 could interact with each other and with the parameters previously determined, leading potentially to a very complex analysis. In fact, we will show that most effects can be treated as isolated from one another, which greatly facilitates the exposition. In the following sections, we will discuss the higher-order microlens effects in the order of their impact on the ground-based light curve, starting with the strongest, i.e., parallax effects (§ 3.1), followed by planetary orbital motion (§ 3.2) and finally the weakest, finite-source effects (§ 3.3.3). To study these effects, we implement Markov chain Monte Carlo (MCMC) with an adaptive step-size Gaussian sampler (Doran & Mueller 2003) to perform the model fitting and obtain the uncertainties of the parameters. The *HST* astrometry is consistent with no $(V-I)$ color-dependent centroid shift in the first epoch and such shift is seen in the second epoch observations (§ 3.4). In addition, the PSF of the source shows no sign of broadening due to the blend, suggesting that the blend is associated with the event (§ 3.5). Therefore, the *HST* observations provide good evidence that the blend is likely due to the lens. In § 3.4, it is shown that, under such an assumption, how the astrometry can be used in conjuncation with finite-source and microlens parallax measurements to constrain the angular Einstein radius and proper motion (§ 3.4). In § 3.5, we discuss using *HST* photometric constraints in the form of χ^2 penalties to the MCMC runs to extract the color and brightness of the blend. The results of these runs, which include all higher-order effects of the ground-based light curve and the *HST* photometric constraints, are summarized as "MCMC A" in Table 1. Subsequently in § 3.6, by making the assumption that the blended light seen by *HST* is due to the lens, we combine all constraints discussed above to obtain physical parameters of the lens star and its planet. The corresponding best-fit model parameters are reported as "MCMC B" in Table 1. The results for the physical parameters from these runs are given in Table 2. Finally we discuss some caveats in the analysis in § 3.7 and § 3.8.

3.1. Microlens Parallax Effects

A point-source static binary-lens model has 6 "geometric-model" parameters: three "single-lens" parameters (t_0, u_0, $t_{\rm E}$), where we define the time of "peak" magnification t_0

and the impact parameter u_0 with respect to the center of mass of the planet-star systems; and three "binary-lens" parameters (q, b, α), where α is the angle between the star-planet axis and the trajectory of the source relative to the lens. In addition, flux parameters are included to account for light coming from the source star (F_s) and the blended light (F_b) for each dataset. In this paper, we extend the fitting by including microlens parallax, orbital motion and finite-source effects. Paper I reported that, within the context of the point-source static binary-lens models, the best-fit wide-binary ($b > 1$) solution is preferred by $\Delta\chi^2 = 22$ over the close-binary ($b < 1$) solution. Remarkably, when we take account of parallax, finite-source and orbital effects, this advantage is no longer as significant. We discuss the wide/close degeneracy with more detail in § 3.6.2.

The microlens parallax effects are parametrized by $\pi_{\rm E,E}$ and $\pi_{\rm E,N}$, following the geocentric parallax formalism by An et al. (2002) and Gould (2004). To properly model the parallax effects, we characterize the "constant acceleration degeneracy" (Smith et al. 2003) by probing models with $u_0 \rightarrow -u_0$ and $\alpha \rightarrow -\alpha$. We find that all other parameters remain essentially unchanged under this form of degeneracy. In the following sections, if not otherwise specified, parameters from models with positive u_0 are adopted.

As shown in Figure 2, microlens parallax is firmly detected in this event at $> 8\sigma$ level. Not surprisingly, the error ellipse of $\boldsymbol{\pi}_{\rm E}$ is elongated toward $\pi_{\rm E,\perp}$, i.e., the direction perpendicular to the position of the Sun at the peak of event, projected onto the plane of the sky (Gould et al. 1994; Poindexter et al. 2005). As a result, $\pi_{\rm E,E}$ is much better determined than $\pi_{\rm E,N}$,

$$\pi_{\rm E,E} = -0.26 \pm 0.05, \quad \pi_{\rm E,N} = -0.34^{+0.24}_{-0.25} \qquad \text{(wide)}, \tag{5}$$

$$\pi_{\rm E,E} = -0.28 \pm 0.05, \quad \pi_{\rm E,N} = -0.39^{+0.25}_{-0.28} \qquad \text{(close)}. \tag{6}$$

Xallarap could provide an alternate explanation of the detected parallax signals. In § 3.8, we find that the best-fit xallarap parameters are consistent with those derived from the Earth's orbit, a result that favors the parallax interpretation.

3.2. Fitting Planetary Orbital Motion

To model orbital motion, we adopt the simplest possible model, with uniform expansion rate $\dot{b}$ in binary separation b and uniform binary rotation rate ω. Because orbital effects are operative only for about 4 days, while the orbital period is the order of 10 years, this is certainly adequate. Interestingly, the orbital motion is more strongly detected for the

close solutions (at $\gtrsim 5.5\sigma$ level) than the wide solutions (at $\sim 3\sigma$ level), and as a result, it significantly lessens the previous preference of the wide solution that was found before orbital motion was taken into account. Further discussions on planetary orbital motion are given in § 3.6.2.

3.3. Finite-source effects and Other Constraints on $\theta_{\rm E}$

3.3.1. Color-Magnitude Diagram

We follow the standard procedure to derive dereddened source color and magnitude from the color-magnitude diagram (CMD) of the observed field. Figure 3 shows the calibrated OGLE CMD (black), with the baseline source displayed as a green point. The $V-I$ color of the source can be determined in a model-independent way from linear regression of the I-band and V-band observations. The I-band magnitude of the source are also precisely determined from the microlens model, and it is hardly affected by any higher-order effects. The center of red clump (red) is at $(V-I, I)_{\rm clump} = (1.89, 15.67)$. The Galactic coordinates of the source are at $(l, b) = (355.58, -3.79)$, where the red clump density peaks behind the Galactic center by 0.15 magnitude (Nishiyama 2005). Hence, we derive $(V-I, I)_{0,\rm clump} = (1.00, 14.37)$, by adopting a Galactic distance $R_0 = 8\,$kpc. We thereby obtain the selective and total extinction toward the source $[E(V-I), A_I] = (0.89, 1.20)$ and thus $R_{VI} = A_V/E(V-I) = 2.35$. The de-reddened color and magnitude of the source is $((V-I), I)_{s,0} = (0.45, 18.31)$. Following the method of Yoo et al. (2004), we transform $(V-I)_0 = 0.45$ to $(V-K)_0 = 0.93$ (Bessell & Brett 1988), and based on the empirical relation between color and surface brightness (Kervella et al. 2004), we obtain the angular size of the source

$$\theta_* = 0.52 \times 10^{0.2(19.51-I_s)} \pm 0.05\,\mu{\rm as}, \tag{7}$$

where I_s is the apparent magnitude of the source in I band. Other features on the CMD shown in Figure 3 are further discussed in § 3.5.

3.3.2. Photometric Systematics of the Auckland Dataset

The Auckland dataset's excellent coverage over the two peaks makes it particularly useful for probing the finite-source effects. Unlike the more drastic "caustics crossings" that occur in some events, the finite-source effects during "cusp approaches" are relatively subtle. Hence one must ensure that the photometry is not affected by systematics at the few percent level when determining $\rho = \theta_*/\theta_{\rm E}$. The Auckland photometry potentially suffer from two major systematic effects.

First, the photometry of constant stars reduced by μFUN's DoPHOT pipeline are found to show sudden "jumps" of up to $\sim 10\%$ when the field crossed the meridian each night. The signs and amplitudes of the "jumps" depend on the stars' positions on the CCD. The Auckland telescope was on a German equatorial mount, and hence the camera underwent a meridian flip. Due to scattered light, the flat-fielded images were not uniform in illumination for point sources, an effect that can be corrected by making "superflats" with photometry of constant stars (Manfroid 1995). We have constructed such "superflats" for each night of Auckland observations using 71 bright isolated comparison stars across the frame. The DoPHOT instrumental magnitude $m_{i,j}$ for star i on frame j is modeled by the following equation:

$$m_{i,j} = m_{0,i} - f(x_{i,j}, y_{i,j}) - Z_j - fwhm_{i,j} \times s_i \tag{8}$$

where $m_{0,i}$ is the corrected magnitude for star i, $f(x, y)$ is a bi-quartic illumination correction as a function of the (x, y) position on the CCD frame with 14 parameters, Z_j is a zero-point parameter associated with each frame (but with Z_1 set to be zero), and s_i is a linear correlation coefficient for the seeing $fwhm_{i,j}$. A least squares fit that recursively rejects 4-σ outliers is performed to minimize χ^2. The best-fit $f(x, y)$ is dominated by the linear terms and has small quadratic terms, while its cubic and quartic terms are negligible. The resulting reduced χ^2 is close to unity, and the "jumps" for all stars are effectively eliminated. We apply the bi-quartic corrections to the images and then reduce the corrected images using the DIA pipeline. The resulting DIA photometry of the microlens target is essentially identical (at the $\sim 1\%$ level) to that from the DIA reductions of the original Auckland images.

As we now show, this is because DIA photometry automatically removes any artifacts produced by the first and second-order illumination distortions if the sources are basically uniformly distributed across the frame. For the first order effect, a meridian flip about the target (which is very close to center of the frame) will induce a change in the flux from the source, but it will also induce a change in the mean flux from all other stars in the frame, which for a linear correction will be the same as the change in position of the "center of light" of the frame light. If the frame sources are uniformly distributed over the frame, the "center of light" will be the center of the frame, which is the same position as the source, therefore introducing no effects. The second order transformation is even under a rotation of 180 degrees, whereas a meridian flip is odd under this transformation. Hence the flip has no effects at second order.

Second, the Auckland observations were un-filtered. The amount of atmospheric extinction differs for stars with different colors. As shown in Figure 3, the source is much bluer than most of the bright stars in the field, which dominate the reference image. So the amount of extinction for the source is different from the average extinction over the whole frame. This difference varies as the airmass changes over time during the observations. Coinciden-

tally, the times of the two peaks were both near maximum airmass when the "differential extinction" effect is expected to be the most severe. To investigate this effect, we match the isolated stars in the Auckland frame with CTIO I and V photometry. Then from their $V-I$ colors, we divide all comparison stars into three categories, those with large ("red"), small ("blue") and intermediate ("green") $V-I$ colors. The source is nearly at the mean color of the "blue" stars. We plot the Auckland magnitudes of stars in each category as a function of airmass and find that stars in each category show consistent trends from one night to the next. Their averages are shown in Figure 4. We thereby derive the following empirical formula to adjust the magnitude for the microlensed source by

$$\Delta\mathrm{Mag} = 0.1(Z - 1.4)\Theta(Z - 1.4), \tag{9}$$

where Z is airmass and Θ is a step function. Then we apply the above "differential extinction" corrections to the "superflat"-adjusted DIA photometry to remove both photometric systematics.

In general, the finite source effects depend on the limb-darkening profile of the source star in the observed passbands. We find below that in this case, the impact proves to be extremely weak. Nevertheless, using the matched Auckland and CTIO stars, we study the difference between Auckland magnitudes and I-band magnitude as a function of $V-I$ color. We find the Auckland clear-filter is close to R-band.

3.3.3. Modeling the Finite-Source Effects

After careful tests that are described immediately below, we determined that all finite source calculations can be carried out to an accuracy of 10^{-4} using the hexadecapole approximation of Gould (2008). This sped up calculations by several orders of magnitude. We began by conducting MCMC simulations using the "loop linking" finite-source code described in Appendix A of Dong et al. (2006). From these simulations, we found the $4.5\,\sigma$ upper bound on the finite-source parameter $\rho(4.5\,\sigma) = 0.001$. We then examined the differences between loop-linking (set at ultra-high precision) and hexadecapole for light curves at this extreme limit and found a maximum difference of 10^{-4}. Based on Claret (2000), we adopt linear limb-darkening coefficients $\Gamma_I = 0.35$ for the I-band observations and $\Gamma_R = 0.43$ for the observations performed in R-band and the clear filters, where the local surface brightness is given by $S(\theta) \propto 1 - \Gamma[1 - 1.5(1 - \theta^2/\theta_*^2)^{1/2}]$. Ten additional MCMC runs are performed with Γ_I and Γ_R that differ from the above values by 0.1 or 0.2. They result in essentially the same probability distributions of ρ. Therefore, the choice of limb-darkening parameters has no effect on the results. The best-fit finite-source model has $\Delta\chi^2 \sim 4$ less than the best-fit

point-source model for the wide-binary solution and $\Delta\chi^2 \sim 2$ improvement over point-source solution for the best-fit close-binary solution. Solutions with $\rho > 0.0009$ are ruled out at more than 3σ. The angular Einstein radius is given by $\theta_{\rm E} = \theta_*/\rho$. Hence, the lack of pronounced finite-source effects yields a 3σ lower limit: $\theta_{\rm E} > 0.6\,{\rm mas}$. The lens-source relative proper motion in the geocentric frame is simply $\mu_{\rm geo} = \theta_{\rm E}/t_{\rm E}$. The posterior probability distributions of $\boldsymbol{\mu}_{\rm geo}$ derived from these MCMC simulations are compared with those derived from astrometry in § 3.4.

3.4. *HST* Astrometry

HST observations were taken at two epochs (HJD = 2453513.6 and HJD = 2453788.2) with the ACS High Resolution Camera (HRC). For each epoch, 4 dithered images were acquired in each of F814W and F555W with individual exposure times of 225s and 315s respectively. The position of the microlens on the *HST* frame is in excellent agreement with its centroid on the OGLE difference image (within $\sim 0.01''$). The closest star to the source is about $0.6''$ away. This implies that the OGLE photometry of the source does not contain additional blended light that would be identifiable from the HST images. Data analysis was carried out using the software program `img2xym_HRC` (Anderson & King 2004) in a manner similar to that described in Bennett et al. (2006). Stars are fitted with an empirical "library" PSF that was derived from well-populated globular cluster fields. These positions are then corrected with precise distortion-correction models (accurate to ~ 0.01 pixel). We adopted the first F555W frame of the first epoch as the reference frame, and used the measured positions of stars in this frame and the frame of each exposure to define a linear transformation between the exposure frame and the reference frame. This allowed us to transform the position of the target star in each exposure into the reference frame, so that we see how the target star had moved relative to the other stars. The centroid positions of the target star in each filter and epoch are shown in Figure 5. For convenience, in this figure, the positions are displayed relative to the average of the centroid positions. The error bars are derived from the internal scatter of the four dithered images. For the first epoch, there is 38% of chance that the centroid offset between F814W and F555W is consistent with zero. This is compatible with the picture that the blend is due to the lens since the first epoch was only about half of the Einstein-radius crossing time after t_0, implying that the lens-source separation induces only a very small centroid offset, well below the *HST* detection limit. For the second epoch, the centroid offset is,

$$\Delta\mathbf{r}_{\rm F814W-F555W,East} = -0.52 \pm 0.20\,{\rm mas}, \qquad \Delta\mathbf{r}_{\rm F814W-F555W,North} = 0.22 \pm 0.20\,{\rm mas}. \quad (10)$$

We also calculate the error in the centroid offsets from the scatter in such offsets among all comparison stars with F555W magnitudes within 0.5 mag of the target and find that it is consistent with the internally-based error quoted above.

At the peak of the event, the angular separation between the lens and the source was negligible, since $u_0 \ll 1$. We therefore fix the angular positions of the lens and source at a common $\boldsymbol{\theta_0}$. From the CMD (Fig. 3), most of the stars in the *HST* field are from the bulge. So we set a reference frame that is fixed with respect to the bulge field at distance D_s. The source and lens positions at time t are then,

$$\begin{aligned} \boldsymbol{\theta_s}(t) &= \boldsymbol{\theta_0} + \boldsymbol{\mu_s}(t - t_0), \\ \boldsymbol{\theta_l}(t) &= \boldsymbol{\theta_0} + \boldsymbol{\mu_l}(t - t_0) + \pi_{\rm rel}[\boldsymbol{s}(t) - \boldsymbol{s}(t_0)], \end{aligned} \tag{11}$$

where $\boldsymbol{s}(t)$ is the Earth-to-Sun vector defined by Gould (2004). Therefore, using equations (3) and (4), one can obtain the centroid position of the lens and the source at time t

$$\begin{aligned} \boldsymbol{\theta_c}(t) &= [1 - f_l(t)]\boldsymbol{\theta_s}(t) + f_l(t)\boldsymbol{\theta_l}(t) \\ &= \boldsymbol{\theta_0} + \boldsymbol{\mu_s}(t - t_0) + f_l(t)[\boldsymbol{\mu}_{\rm geo}(t - t_0) + \pi_{\rm rel}\Delta\boldsymbol{s}(t)] \end{aligned} \tag{12}$$

where $f_l(t)$ is the fraction of the total flux due to the lens and $\Delta\mathbf{s}(t)$ is the positional offset of the Sun in the geocentric frame at t from t_0 given by Gould (2004).

The centroid offset between the two passbands, F814W and F555W, is related to the properties of the system by,

$$\Delta\boldsymbol{\theta}_c(t)_{\rm F814W-F555W} = [f(t)_{l,\rm F814W} - f(t)_{l,555\rm W}] \times [\boldsymbol{\mu}_{\rm geo}(t - t_0) + \pi_{\rm rel}\Delta\boldsymbol{s}(t)]. \tag{13}$$

The difference of the blend's fractional flux between F814W and F555W is obtained from "MCMC A" described in § 3.5. Consequently, under the assumption that the blend is the lens, we can use the measurement of the second-epoch *HST* centroid offset to estimate the relative proper motion from equation (13) for a given $\pi_{\rm rel}$. For purposes of illustration, we temporarily adopt $\pi_{\rm rel} = 0.2$ when calculating the probability distribution of $\boldsymbol{\mu}_{\rm geo}$ (black contours in the upper panels of Fig. 6). The centroid shift generally favors faster relative proper motion than that derived from the source size measurement (green contours in Fig. 6), but the difference is only at the $\sim 1\sigma$ level. We then get a joint probability distribution of $\boldsymbol{\mu}_{\rm geo}$ from both finite-source effects and astrometry, which is shown as the red contours in the upper panels of Figure 6.

We then derive the distribution of the $\boldsymbol{\mu}_{\rm geo}$ position angle $\phi_{\boldsymbol{\mu}_{\rm geo}}$ (North through East), which is shown by the red histograms in the lower panels of Figure 6. Since the direction of the lens-source relative proper motion $\boldsymbol{\mu}_{\rm geo}$ is the same as that of the microlens parallax

$\boldsymbol{\pi}_{\rm E}$ in the geocentric frame, we have an independent check on the $\phi\boldsymbol{\mu}_{\rm geo}$ from our parallax measurements, whose distribution is plotted as blue histograms in Figure 6. Both constraints favor the lens-source proper motion to be generally West, but they disagree in the North-South component for which both constraints are weaker. The disagreements between two histograms is at about $\sim 2.5\sigma$ level.

3.5. "Seeing" the Blend with *HST*

If the blend were not the lens, the PSF of the source would likely be broadened by the blended star. We examine the *HST* F814W images of the target and 45 nearby stars with similar brightness for each available exposure. We fit them with the library PSF produced by Anderson & King (2004). In order to account for breathing-related changes of focus, we fit each of these 45 nearby stars with the library PSF, and construct a residual PSF that can be added to the library PSF to produce a PSF that is tailor-made for each exposure. For both epochs, the source-blend combination shows no detectable broadening relative to the PSFs of other isolated stars in the field. From the ground-based light curve, it is already known that $\sim 16\%$ of this light comes from the blend. We add simulated stars with the same flux as the blended light from 0 to 2.0 pixels away from the center of the source. We find that the blend would have produced detectable broadening of the PSF if it were more than 15 mas apart from the source at the second epoch. Hence, the source-blend separation must then be less than about 15 mas. From the *HST* image itself, the density of ambient stars at similar magnitudes is $\lesssim 1\,{\rm arcsec}^{-2}$. The probability of a chance interloper is therefore $< 0.07\%$, implying that the blended light is almost certainly associated with the event, i.e., either the lens itself, a companion to the lens, or a companion to the source. Both of the latter options are further constrained in § 3.7 where, in particular, we essentially rule out the lens-companion scenario.

As discussed in § 2, the blended flux in I is relatively well determined from the ground-based OGLE data alone, but the blended V flux is poorly determined, primarily because the systematic uncertainty in the zero point of the baseline flux (determined from PSF fitting) is of the same order as the blended flux. Because the *HST* image is very sparse, there is essentially no zero-point error in the *HST* V band flux. The problem is how to divide the baseline V flux into source and blend fluxes, $F_{\rm base} = F_s + F_b$.

The standard method of doing this decomposition would be to incorporate the *HST* V light curve into the overall fit, which would automatically yield the required decomposition.

Since this "light curve" consists of two points, the "fit" can be expressed analytically

$$F_s = \frac{F(t_1) - F(t_2)}{A_1 - 1}, \qquad F_b = F(t_2) - F_s. \tag{14}$$

where we have made the approximation that the second observation is at baseline. Let us then estimate the resulting errors in F_s and F_b, ignoring for the moment that there is some uncertainty in A_1 due to uncertainties in the general model. Each of the individual flux measurement is determined from 4 separate sub-exposures, and this permits estimates of the errors from the respective scatters. These are $\sigma_1 = 0.015$ and $\sigma_2 = 0.025$ mag. Hence, the fractional error in F_s is $(2.5/\ln 10)\sigma(F_s)/F_s = [\sigma_1^2(A_1 + r)^2 + \sigma_2^2(1 + r)^2]^{1/2}/(A_1 - 1)$, where $r \equiv F_b/F_s$. Adopting, for purposes of illustration, $A_1 = 2$ and $r = 0.1$, this implies an error $\sigma(V_{s,HST})$ of 0.045 mag. This may not seem very large, but after the subtraction in equation (14), it implies an error $\sigma(V_{b,HST}) \sim \sigma(V_{s,HST})/r \sim 0.45$ mag. Hence, we undertake an alternate approach.

Because the *HST* and OGLE V filters have very nearly the same wavelength center, $V_{s,HST}$ should be nearly identical to $V_{s,\mathrm{OGLE}}$ up to a possible zero-point offset on their respective magnitude scales. Because the OGLE data contain many more points during the event, some at much higher magnification than the single *HST* event point, $V_{s,\mathrm{OGLE}}$ is determined extremely well (for fixed microlensing model), much better than the 0.045 mag error for $V_{s,HST}$. Thus, if the zero-point offset between the two systems can be determined to better than 0.045 mags, this method will be superior. Although the I-band blend is much better measured than the V-band blend from the ground-based data, for consistency we determine the zero-point offset in I by the same procedure.

Figure 7 shows differences between OGLE and *HST* V magnitudes for matched stars in the *HST* image. The error for each star and observatory is determined from the scatter among measurements of that star. We consider only points with $V < 19.5$ because at fainter magnitudes the scatter grows considerably. Each star was inspected on the *HST* images, and those that would be significantly blended on the OGLE image were eliminated. The remaining points are fit to an average offset by adding a "cosmic error" in quadrature to the errors shown. We carry out this calculation twice, once including the "outlier" (shown as a filled circle) and once with this object excluded. For V-band, we find offsets of $V_{HST} - V_{\mathrm{OGLE}} = 0.17 \pm 0.01$ and 0.18 ± 0.01, respectively. We adopt the following V-band offset

$$\Delta V = V_{HST} - V_{\mathrm{OGLE}} = 0.18 \pm 0.01. \tag{15}$$

A similar analysis of I band leads to

$$\Delta I = I_{HST} - I_{\mathrm{OGLE}} = 0.08 \pm 0.01. \tag{16}$$

We find no obvious color terms for either V-band or I-band transformations. As a check, we perform linear-regression to compare the OGLE and *HST* $(V-I)$ colors, and we find they agree within 0.01 mag, which further confirms the color terms are unlikely to be significant in the above transformations.

We proceed as follows to make *HST*-based MCMC ("MCMC A") estimates of $V_{b,\rm OGLE}$ and $I_{b,\rm OGLE}$ that place the blending star on the OGLE-based CMD. Since flux parameters are linear, they are often left free and fitted by linear least-squares minimization, which significantly accelerates the computations. However, for "MCMC A", the source fluxes from OGLE and *HST* are treated as independent MCMC parameters so that they can help align the two photometric systems as described below. Since *HST* blended light is not affected by light from ambient stars (as OGLE is), we also leave *HST* blended fluxes as independent. Therefore, in "MCMC A", we include the following independent MCMC flux parameters, $F_{I,s,\rm OGLE}$, $F_{V,s,\rm OGLE}$, $F_{I,s,HST}$, $F_{V,s,HST}$, $F_{I,b,HST}$, and $F_{V,b,HST}$, which for convenience we express here as magnitudes. For each model on the chain, we add to the light-curve based χ^2 two additional terms $\Delta\chi^2_V = (V_{s,HST} - V_{s,\rm OGLE} - \Delta V)^2/[\sigma(\Delta V)]^2$ and $\Delta\chi^2_I = (I_{s,HST} - I_{s,\rm OGLE} - \Delta I)^2/[\sigma(\Delta I)]^2$ to enforce the measured offset between the two systems. Finally, we evaluate the V-band blended flux from *HST* and convert it to OGLE system, $V_{b,\rm OGLE/HST} = V_{s,\rm OGLE} - V_{s,HST} + V_{b,HST}$ (and similarly for I band), where all three terms on the rhs are the individual Monte Carlo realizations of the respective parameters.

The result is shown in Figure 3, in which the blend (magenta) is placed on the OGLE CMD. Also shown, in cyan points, is *HST* photometry (aligned to the OGLE system) of the stars in the ACS subfield of the OGLE field. Although this field is much smaller, its stars trace the main sequence to much fainter magnitudes. The blend falls well within the bulge main sequence revealed by the *HST* stars on the CMD, so naively the blend can be interpreted as being in the bulge. Hence, this diagram is, in itself, most simply explained by the blend being a bulge lens or a binary companion of the source. However, the measurement of $V-I$ color has relatively large uncertainty, and it is also consistent with the blend being the lens (or a companion to it) several kpc in front of the bulge, provided the blend is somewhat redder than indicated by the best-fit value of its color. In the following section, we assume the blended light seen by *HST* is the foreground lens star, and the *HST* photometry is combined with other information to put constraints on the lens star under this assumption.

3.6. Final Physical Constraints on the Lens and Planet

3.6.1. Constraints on a Luminous Lens

In the foregoing, we have discussed two types of constraints on the host star properties: the first class of constraints, consisting of independent measurements of $\boldsymbol{\pi_{\rm E}}$, $\theta_{\rm E}$ and $\boldsymbol{\mu}$, relate the microlens parameters to the physical parameters of the lens; the second class are *HST* and ground-based observations that determine the photometric properties of the blend.

In this section, we first describe a new set of MCMC simulations taking all these constraints into account. Similarly to what is done to include *HST* photometry in the "MCMC A" (see § 3.5), we incorporate *HST* astrometry constraints by adding χ^2 penalties to the fittings. For a given set of microlens parameters, we can derive the physical parameters, namely, M, $\pi_{\rm rel}$, $\boldsymbol{\mu}_{\rm geo}$, and so calculate $\rho = \theta_*/\theta_{\rm E}$ (from eq. [1]) and the F814W − F555W centroid offset (from eq. [13]). Then we assign the χ^2 penalties based on the observed centroid offset from § 3.4. In this way, the MCMC simulations simultaneously include all microlens constraints on the lens properties. The posterior probability distribution of M and $\pi_{\rm rel}$ are plotted in Figure 8. The $\pi_{\rm rel}$ determination very strongly excludes a bulge ($\pi_{\rm rel} \lesssim 0.05$) lens. Note that by incorporating *HST* astrometry, we are implicitly assuming that the blend is the lens.

If the blend is indeed the lens itself, we can also estimate its mass and distance from the measured color and magnitude of the blend. In doing so, we use theoretical stellar isochrones (M. Pinsonneault 2007, private communication) incorporating the color-temperature relation by Lejeune et al. (1997, 1998). We first use an isochrone that has solar metal abundance, with stellar masses ranging from $0.25 M_\odot - 1.0 M_\odot$, and an age of 4 Gyrs. The variation in stellar brightness due to stellar age is negligible for our purpose. Extinction is modeled as a function of D_l by $dA_I/dD_l = (0.4\,{\rm kpc}^{-1}) \exp(-wD_l)$, where w is set to be $0.31\,{\rm kpc}^{-1}$ so that the observed value $A_I(8.6\,{\rm kpc}) = 1.20$ (as derived from CMD discussed in § 3.3.1) is reproduced. Again, the distance to the source is assumed to be 8.6 kpc, implying $\pi_s = 0.116\,{\rm mas}$, and hence that the lens distance is $D_l/{\rm kpc} = {\rm mas}/(\pi_{\rm rel} + \pi_s)$. In Figure 8, we show the lens mass M and relative parallax $\pi_{\rm rel}$ derived from the isochrone that correspond to the observed I-band magnitude $I = 21.3$ in black line and a series of $V-I$ values $V-I = 1.9$ (best estimate), 2.0 ($0.5\,\sigma$), 2.2 ($1\,\sigma$), 2.4 ($1.5\,\sigma$) and 2.6 ($2\,\sigma$) as black points. The observed color is in modest disagreement $< 2\sigma$ with the mass and distance of the lens at solar metallicity. We also show analogous trajectories for [M/H] = −0.5 (red) and [M/H] = −1.0 (green). The level of agreement changes only very weakly with metallicity.

We then include the isochrone information in a new set of MCMC runs ("MCMC B"). To do so, the *HST* blended fluxes in I and V bands can no longer be treated as independent

MCMC parameters. Instead, based on the isochrone with solar metallicity, the lens $V-I$ color and I magnitude are predicted at the lens mass determined from MCMC parameters. Then the *HST* I-band and V-band fluxes are fixed at the predicted values in the fitting for each MCMC realization.

Figure 9 illustrates the constraints on M and $\pi_{\rm rel}$ from the MCMC, which are essentially the same for both wide-binary (solid contours) and close-binary (dashed contours) solutions:

$$M = 0.46 \pm 0.04\,M_\odot, \qquad \pi_{\rm rel} = 0.19 \pm 0.03\,{\rm mas}. \tag{17}$$

Assuming the source distance at 8.6 kpc, the $\pi_{\rm rel}$ estimates translate to the following lens distance measurement:

$$D_l = 3.3 \pm 0.4\,{\rm kpc}. \tag{18}$$

Furthermore, we can derive constraints on the planet mass M_p and the projected separation between the planet and the lens star $r_\perp$,

$$M_p = 3.5 \pm 0.3 M_{\rm Jupiter}, \qquad r_\perp = 3.6 \pm 0.2{\rm AU} \qquad ({\rm wide}), \tag{19}$$

and

$$M_p = 3.3 \pm 0.3 M_{\rm Jupiter}, \qquad r_\perp = 2.1 \pm 0.1{\rm AU} \qquad ({\rm close}). \tag{20}$$

The wide solution is slightly preferred over close solution by $\Delta\chi^2 \sim 4$.

To examine possible uncertainties in extinction estimates, we reran our MCMC with A_I and A_V that are 10% higher and lower than the fiducial values. These runs result in very similar estimates as when adopting the fiducial values.

From equation (12), one can easily obtain the centroid shift between two epochs in a given passband[1],

$$\begin{aligned} \boldsymbol{\theta_c}(t_2) - \boldsymbol{\theta_c}(t_1) \;\; = \;\; & \boldsymbol{\mu_s}(t_2 - t_1) + \boldsymbol{\mu}_{\rm geo}[f_l(t_2)(t_2 - t_0) - f_l(t_1)(t_1 - t_0)] \\ & + \pi_{\rm rel}[f_l(t_2)\Delta\boldsymbol{s}(t_2) - f_l(t_1)\Delta\boldsymbol{s}(t_1)] \end{aligned} \tag{21}$$

Because $\boldsymbol{\mu}_{\rm geo}$, $\pi_{\rm rel}$ and f_l in a given passband can be extracted from the MCMC realizations ("MCMC B"), we can use the above equation to measure the source proper motion by

[1]The angular separations between the source and the lens are $\sim 0.47\theta_{\rm E}$ and $\sim 4.4\theta_{\rm E}$ for the two *HST* epochs, respectively. Thus the angular position offsets between the centroids of the source images and the source are both $\sim 0.21\theta_{\rm E}$ and the directions of the offset relative to the source are almost the same due to the small impact parameter u_0. The difference between lens flux fractions of the two epochs are about 7% in I band, so the offsets can be confidently ignored in deriving the source proper motion using the relative astrometry in F814W at two different epochs.

making use of the centroid shift in F814W between two epochs. The source proper motion with respect to the mean motion of stars in the *HST* field is measured to be

$$\boldsymbol{\mu_s} = (\mu_{s,E},\, \mu_{s,N}) = (2.2 \pm 0.3,\, -0.3^{+0.3}_{-0.6})\,\mathrm{mas\,yr^{-1}}. \tag{22}$$

We obtain similar results with F555W, but with understandably larger errorbars since the astrometry is more precise for the microlens in F814W.

Combining equations (3) and (4), the lens proper motion in the heliocentric frame is therefore

$$\boldsymbol{\mu}_l = \boldsymbol{\mu}_{\rm geo} + \boldsymbol{\mu}_s + \frac{\boldsymbol{v}_\oplus \pi_{\rm rel}}{\rm AU}, \tag{23}$$

For each MCMC realization, $\pi_{\rm rel}$ is known, so we can convert the lens proper motion to the velocity of the lens in the heliocentric frame $\boldsymbol{v}_{l,\rm hel}$ and also in the frame of local standard of rest $\boldsymbol{v}_{l,\rm LSR}$ (we ignore the rotation of the galactic bulge). The lens velocity in the LSR is estimated to be $v_{l,\rm LSR} = 103 \pm 14\,\mathrm{km\,s^{-1}}$. This raises the possibility of the lens being in the thick disk, in which the stars are typically metal-poor. As shown in Figure 8, the constraints we have cannot resolve the metallicity of the lens star.

3.6.2. Planetary Orbital Motion

Wide/Close Degeneracy Binary-lens light curves in general exhibit a well-known "close-wide" symmetry (Dominik 1999; An 2005). Even for some well-covered caustics-crossing events (e.g., Albrow et al. 1999), there are quite degenerate sets of solutions between wide and close binaries. In Paper I, we found that the best-fit point-source wide-binary solution was preferred over close-binary solutions by $\Delta\chi^2 \sim 22$. But this did not necessarily mean that the wide-close binary degeneracy was broken, since the two classes of binaries may be influenced differently by higher-order effects. We find that the χ^2 difference between best-fit wide and close solutions is only ~ 3 from "MCMC A" and about 4 from "MCMC B".

However, orbital motion of the planet is subject to additional dynamical constraints: the projected velocity of the planet should be no greater than the escape velocity of the system: $v_\perp \leq v_{\rm esc}$, where,

$$v_\perp = \sqrt{\dot{b}^2 + (\omega b)^2}\frac{\rm AU}{\pi_l}\theta_{\rm E}, \tag{24}$$

$$v_{\rm esc} = \sqrt{\frac{2GM}{r}} \leq v_{\rm esc,\perp} \equiv \sqrt{\frac{2GM}{b\theta_{\rm E} D_l}} = \sqrt{\frac{\pi_l}{2b\pi_{\rm E}}}c, \tag{25}$$

and where r is the instantaneous 3-dimensional planet-star physical separation. Note that in the last step, we have used equation (1).

We then calculate the probability distribution of the ratio

$$\frac{v_\perp^2}{v_{\rm esc,\perp}^2} = 2\frac{\rm AU^2}{c^2}\frac{b^3[(\dot{b}/b)^2+\omega^2]}{[\pi_{\rm E}+(\pi_s/\theta_{\rm E})]^3}\frac{\pi_{\rm E}}{\theta_{\rm E}} \tag{26}$$

for an ensemble of MCMC realizations for both wide and close solutions. Figure 10 shows probability distributions of the projected velocity $r_\perp\boldsymbol{\gamma}$ in the units of critical velocity $v_{\rm c,\perp}$, where $r_\perp\boldsymbol{\gamma}$ is the instantaneous velocity of the planet on the sky, which is further discussed in Appendix A and $v_{\rm c,\perp} = v_{\rm esc,\perp}/\sqrt{2}$. The dotted circle encloses the solutions that are allowed by the escape velocity criteria, and the solutions that are inside the solid line are consistent with circular orbital motion. We find that neither close nor wide solutions are excluded by these constraints. We conclude that the wide-binary solution is slightly favored, although the close-binary solution is not ruled out.

Circular Planetary Orbits and Planetary Parameters Planetary deviations in microlensing light curves are intrinsically short, so in most cases, only the instantaneous projected distance between the planet and the host star can be extracted. As shown in § 3.6.2, for this event, we tentatively measure the instantaneous projected velocity of the planet thanks to the relatively long (~ 4 days) duration of the planetary signal. One cannot solve for the full set of orbital parameters just from the instantaneous projected position and velocity. However, as we show in Appendix A, we can tentatively derive orbital parameters by assuming the planet follows a circular orbit around the host star. In Figure 11, we show the probability distributions of the semi-major axis, inclination, amplitude of radial velocity, and equilibrium temperature of the planet derived from "MCMC B" for both wide and close solutions. In calculating these probabilities, we assign a flat (Öpik's Law) prior for the semi-major axis and assume that the orbits are randomly oriented, that is, with a uniform prior on $\cos i$.

3.7. Constraints on a Non-Luminous Lens

In § 3.5, we noted that the blended light must lie within 15 mas of the source: otherwise the *HST* images would appear extended. We argued that the blended light must be associated with the event (either the lens itself or a companion to either the source or lens), since the chance of such an alignment by a random field star is $< 0.07\%$. In fact, even stronger constraints can be placed on the blend-source separation using the arguments of § 3.4. These are somewhat more complicated and depend on the blend-source relative parallax, so we do not consider the general case (which would only be of interest to further reduce the already

very low probability of a random interloper) but restrict attention to companions of the source and lens. We begin with the simpler source-companion case.

3.7.1. Blend As Source Companion

As we reported in § 3.4, there were two *HST* measurements of the astrometric offset between the V and I light centroids, dating from 0.09 and 0.84 years after peak, respectively. In that section, we examined the implications of these measurements under the hypothesis that the blend is the lens. We therefore ignored the first measurement because the lens source separation at that epoch is much better constrained by the microlensing event itself than by the astrometric measurement. However, as we are now examining the hypothesis that the blend is a companion to the source, both epochs must be considered equally. Most of the weight (86%) comes from the second observation, partly because the astrometric errors are slightly smaller, but mainly because the blend contributes about twice the fractional light, which itself reduces the error on the inferred separation by a factor of 2. Under this hypothesis, we find a best-fit source-companion separation of 5 mas, with a companion position angle (north through east) of 280°. The (isotropic) error is 3 mas. Approximating the companion-source relative motion as rectilinear, this measurement strictly applies to an epoch 0.75 years after the event, but of course the intrinsic source-companion relative motion must be very small compared to the errors in this measurement.

There would be nothing unusual about such a source-companion projected separation, roughly 40 ± 25 AU in physical units. Indeed, the local G-star binary distribution function peaks close to this value (Duquennoy & Mayor 1991).

The derived separation is also marginally consistent with the companion generating a xallarap signal that mimics the parallax signal in our dominant interpretation. The semi-major axis of the orbit would have to be about 0.8 AU to mimic the 1-year period of the Earth, which corresponds to a maximum angular separation of about 100 μas, which is compatible with the astrometric measurements at the $1.6\,\sigma$ level.

Another potential constraint comes from comparing the color difference with the magnitude difference of the source and blend. We find that the source is about 0.5 ± 0.5 mag too bright to be on the same main sequence. However, first, this is only a $1\,\sigma$ difference, which is not significant. Second, both the sign and magnitude of the difference are compatible with the source being a slightly evolved turnoff star, which is consistent with its color.

The only present evidence against the source-companion hypothesis is that the astrometric offset between V and I *HST* images changes between the two epochs, and that the

direction and amplitude of this change is consistent with other evidence for the proper motion of the lens. Since this is only a $2.5\,\sigma$ effect, it cannot be regarded as conclusive. However, additional *HST* observations at a later epoch could definitively confirm or rule out this hypothesis.

3.7.2. Blend As Lens Companion

A similar, but somewhat more complicated line of reasoning essentially rules out the hypothesis that the blend is a companion to the lens, at least if the lens is luminous. The primary difference is that the event itself places very strong lower limits on how close a companion can be to the lens.

A companion with separation (in units of $\theta_{\rm E}$) $b \gg 1$ induces a Chang-Refsdal (1979) caustic, which is fully characterized by the gravitational shear $\gamma = q/b^2$. We find that the light-curve distortions induced by this shear would be easily noticed unless $\gamma < 0.0035$, i.e.,

$$\gamma = \frac{q_c}{b_c^2} = \frac{q_c \theta_{\rm E}^2}{\theta_c^2} < 0.0035, \tag{27}$$

where $q_c = M_c/M$ is the ratio of the companion mass to the lens mass and $b_c = \theta_c/\theta_{\rm E}$ is the ratio of the lens-companion separation to the Einstein radius. Equivalently,

$$\theta_c > 19\Big(\frac{q_c}{1.3}\Big)^{1/2}\theta_{\rm E}. \tag{28}$$

Here, we have normalized q_c to the minimum mass ratio required for the companion to dominate the light assuming that both are main-sequence stars. (We will also consider completely dark lenses below).

We now show that equation (28) is inconsistent with the astrometric data. If a lens companion is assumed to generate the blend light, then essentially the same line of reasoning given in § 3.7.1 implies that 0.75 years after the event, this companion lies 5 mas from the source, at position angle 280° and with isotropic error of 3 mas. The one wrinkle is that we should now take account of the relative-parallax term in equation (13), whereas this was identically zero (and so was ignored) for the source-companion case. However, this term is only about $1.8\pi_{\rm rel}$ and hence is quite small compared to the measurement errors for typical $\pi_{\rm rel} \lesssim 0.2$mas. We will therefore ignore this term in the interest of simplicity, except when we explicitly consider the case of large $\pi_{\rm rel}$ further below.

Of course, the lens itself is moving during this interval. From the parallax measurement alone (i.e. without attributing the V/I astrometric displacement to lens motion), it is known

that the lens is moving in the same general direction, i.e., with position angle roughly 210°. In assessing the amplitude of this motion we consider only the constraints from finite-source effects (and ignore the astrometric displacement). These constraints yield a hard lower limit on $\theta_{\rm E}$ (from lack of pronounced finite-source effects) of $\theta_{\rm E} > 0.6\,{\rm mas}$, which corresponds to a proper motion $\mu = 3.1\,{\rm mas\,yr^{-1}}$. At this extreme value (and allowing for $2\,\sigma$ uncertainty in the direction of lens motion as well in the measurement of the companion position), the maximum lens-companion separation is 11.4 mas (i.e., $19\,\theta_{\rm E}$), which is just ruled out by equation (28). At larger $\theta_{\rm E}$, the lens-companion scenario is excluded more robustly. For example, in the limit of large $\theta_{\rm E}$, we have $\theta_c = \mu \times 0.75\,{\rm yr} = \theta_{\rm E}(0.75\,{\rm yr}/t_{\rm E}) = 4\theta_{\rm E}$, which is clearly ruled out by equation (28).

Then we note that any scenario involving values of $\pi_{\rm rel}$ that are large enough that they cannot be ignored in this analysis ($\pi_{\rm rel} \gtrsim 0.5\,{\rm mas}$), must also have very large $\theta_{\rm E} = \pi_{\rm rel}/\pi_{\rm E} \gtrsim 1\,{\rm mas}$, a regime in which the lens-companion is easily excluded.

The one major loophole to this argument is that the lens may be a stellar remnant (white dwarf, neutron star, or black hole), in which case it could be more massive than the companion despite the latter's greater luminosity.

3.8. Xallarap Effects and Binary Source

Binary source motion can give rise to distortions of the light curve, called "xallarap" effects. One can always find a set of xallarap parameters to perfectly mimic parallax distortions caused by the Earth's motion (Smith et al. 2003). However, it is a priori unlikely for the binary source to have such parameters, so if the parallax signal is real, one would expect the xallarap fits to converge to the Earth parameters. For simplicity, we assume that the binary source is in circular orbit. We extensively search the parameter space on a grid of 5 xallarap parameters, namely, the period of binary motion P, the phase λ and complement of inclination β of the binary orbit, which corresponds to the ecliptic longitude and latitude in the parallax interpretation of the light curve, as well as $(\chi_{\rm E,E}, \chi_{\rm E,N})$, which are the counterparts of $(\pi_{\rm E,E}, \pi_{\rm E,N})$ of the microlens parallax. We take advantage of the two exact degeneracies found by Poindexter et al. (2005) to reduce the range of the parameter search. One exact degeneracy takes $\lambda' = \lambda + \pi$ and $\boldsymbol{\chi}_E{}' = -\boldsymbol{\chi}_E$, while all other parameters remain the same. The other takes $\beta' = -\beta$, $u_0{}' = -u_0$ and $\chi'_{E,N} = -\chi_{E,N}$ (the sign of α should be changed accordingly as well). Therefore we restrict our search to solutions with positive u_0 and with $\pi \le \lambda \le 2\pi$. In modeling xallarap, planetary orbital motion is neglected. In Figure 12, the χ^2 distribution for best-fit xallarap solutions as a function of period is displayed in a dotted line, and the xallarap solution with a period of 1 year has a $\Delta\chi^2 \sim 0.5$ larger

than the best-fit at 0.9 year. Figure 13 shows that, for the xallarap solutions with period of 1 year, the best-fit has a $\Delta\chi^2 \sim 3.2$ less than the best-fit parallax solution (displayed as a black circle point) and its orbital parameters are close to the ecliptic coordinates of event ($\lambda = 268°$, $\beta = -11°$). Therefore, the overall best-fit xallarap solution has $\Delta\chi^2 = 3.7$ smaller than that of the parallax solution (whose χ^2 value is displayed as a filled dot in Fig. 12) for 3 extra degrees of freedom, which gives a probability of 30%. The close proximity between the best-fit xallarap parameters and those of the Earth can be regarded as good evidence for the parallax interpretation. The slight preference of xallarap could simply be statistical fluctuation or reflect low-level systematics in the light curve (commonly found in the analysis by Poindexter et al. 2005).

We also devise another test on the plausibility of xallarap. In § 3.5, we argued that the blend is unlikely to be a random interloper unrelated to either the source or the lens. If the source were in a binary, then the blend would naturally be explained as the companion of the source star. Then from the blend's position on the CMD, its mass would be $m_c \sim 0.9\,M_\odot$. By definition, $\chi_{\rm E}$ is the size of the source's orbit a_s in the units of $\hat{r}_{\rm E}$ (the Einstein radius projected on the source plane),

$$\chi_{\rm E} = \frac{a_s}{\hat{r}_{\rm E}} = \frac{a m_c}{(m_c + m_s)\hat{r}_{\rm E}}, \tag{29}$$

where a is the semi-major axis of the binary orbit, and m_s and m_c are the masses of the source and its companion. Then we apply Kepler's Third Law:

$$\left(\frac{P}{\rm yr}\right)^2 \frac{m_c^3}{M_\odot (m_c + m_s)^2} = \left(\frac{\chi_{\rm E}\hat{r}_{\rm E}}{\rm AU}\right)^3. \tag{30}$$

Once the masses of the source and companion are known, the product of $\chi_{\rm E}$ and $\hat{r}_{\rm E}$ are determined for a given binary orbital period P. And in the present case, $\hat{r}_{\rm E}/{\rm AU} = \theta_{\rm E} D_s = \theta_*/\rho D_s = 4.5 \times 10^{-3}/\rho$. By adopting $m_s = 1 M_\odot$, $m_c = 0.9 M_\odot$, for each set of P and ρ, there is a uniquely determined $\chi_{\rm E}$ from equation (30). We then apply this constraint in the xallarap fitting for a series of periods. The minimum χ^2s for each period from the fittings are shown in solid line in Figure 12. The best-fit solution has $\Delta\chi^2 \sim 1.0$ less than the best-fit parallax solution for two extra degrees of freedom. Although as compared to the test described in the previous paragraph, the current test implies a higher probability that the data are explained by parallax (rather than xallarap) effects, it still does not rule out xallarap.

4. Summary and Future Prospects

Our primary interpretation of the OGLE-2005-BLG-071 data assumes that the light-curve distortions are due to parallax rather than xallarap and that the blended light is due to the lens itself rather than a companion to the source. Under these assumptions, the lens is fairly tightly constrained to be a foreground M dwarf, with mass $M = 0.46 \pm 0.04\,M_\odot$ and distance $D_l = 3.3 \pm 0.4\,\mathrm{kpc}$, which has thick-disk kinematics ($v_{\rm LSR} \sim 103\,\mathrm{km\,s^{-1}}$). As we discuss below, future observations might help to constrain its metallicity. The microlens modeling suffers from a well-known wide-close binary degeneracy, and the best-fit wide-binary solutions are slightly favored over the close-binary solutions. For the wide-binary model, we obtain a planet of mass $M_p = 3.5 \pm 0.3\,M_{\rm Jupiter}$ at projected separation $r_\perp = 3.6 \pm 0.2\,\mathrm{AU}$. The planet then has an equilibrium temperature of about $T = 50$ K, i.e. similar to Neptune. In the degenerate close-binary solutions, the planet is closer to the star and so hotter, and the estimates are: $M_p = 3.3 \pm 0.3\,M_{\rm Jupiter}$, $r_\perp = 2.1 \pm 0.1\,\mathrm{AU}$ and $T \sim 68$ K.

As we have explored in considerable detail, it is possible that one or both of these assumptions is incorrect. However, future astrometric measurements that are made after the lens and source have had a chance to separate, will largely resolve both ambiguities. Moreover such measurements will put much tighter constraints on the metallicity of the lens (assuming it proves to be the blended light).

First, the astrometric measurements made 0.84 yr after the event detected motion suggests that there was still 1.7% chance that the blend did not move relative to the source. A later measurement that detected this motion at higher confidence would rule out the hypothesis that the blend is a companion to the source. We argued in § 3.7.1 that the blend could not be a companion to a main-sequence lens. Therefore, the only possibilities that would remain are that the lens is the blend, that the lens is a remnant (e.g., white dwarf), or that the blend is a random interloper (probability $< 10^{-3}$). As we briefly summarize below, a future astrometric measurement could strongly constrain the remnant-lens hypothesis as well.

Of course, it is also possible that future astrometry will reveal that the blend is not moving with respect to the source, in which case the blend would be a companion to the source. Thus, either way, these measurements would largely resolve the nature of the blended light.

Second, by identifying the nature of blend, these measurements will largely, but not entirely, resolve the issue of parallax vs. xallarap. If the blend proves not to be associated with the source, then any xallarap-inducing companion would have to be considerably less

luminous, and so (unless it were a neutron star) less massive than the $m_c = 0.9\,M_\odot$ that we assumed in evaluating equation (30). Moreover, stronger constraints on $\hat{r}_{\rm E}$ (rhs of eq. [30]) would be available from the astrometric measurements. Hence, the xallarap option would be either excluded or very strongly constrained by this test.

On the other hand, if the blend were confirmed to be a source companion, then essentially all higher-order constraints on the nature of the lens would disappear. The parallax "measurement" would then very plausibly be explained by xallarap, while the "extra information" about $\theta_{\rm E}$ that is presently assumed to come from the blend proper-motion measurement would likewise evaporate.

These considerations argue strongly for making a future high-precision astrometric measurement. Recall that in the *HST* measurements reported in § 3.5, the source and blend were not separately resolved: the relative motion was inferred from the offset between the V and I centroids, which are displaced because the source and blend have different colors. Due to its well-controlled PSF, *HST* is capable of detecting the broadening of the PSF even if the separation of the lens and source is a fraction of the FWHM. Assuming that the proper motion is $\mu_{\rm geo} \sim 4.4\,{\rm mas\,yr^{-1}}$, and based on our simulations in § 3.5, such broadening would be confidently detectable about 5 years after the event (see also Bennett et al. 2007 for analytic PSF broadening estimates). Ten years after the event, the net displacement would be $\sim 40\,{\rm mas}$. This compares to a diffraction limited FWHM of 40 mas for H band on a ground-based 10m telescope and would therefore enable full resolution. The $I - H$ color of the source is extremely well determined (0.01 mag) from simultaneous I and H data taken during the event from the CTIO/SMARTS 1.3m in Chile. Hence, the flux allocation of the partially or fully resolved blend and source stars would be known. The direct detection of a partially or fully resolved lens will provide precise photometric and astrometry measurements (see Kozłowski et al. 2007 for one such example), which will enable much tighter constraints on the mass, distance and projected velocity of the lens. It also opens up the possibility of determining the metallicity of the host star by taking into account of both non-photometric and photometric constraints. If, as indicated by the projected velocity measurement, it is a thick-disk star, then it will be the first such star found to harbor a planet.

As remarked above, a definitive detection of the blend's proper motion would still leave open the possibility that it was a companion to the lens, not the lens itself. In this case, the lens would have to be a remnant. Without going into detail, the astrometric measurement would simultaneously improve the blend color measurement as well as giving a proper-motion estimate (albeit with large errors because the blend-source offset at the peak of the event would then not be known). It could then be asked whether the parallax, proper-motion, and photometric data could be consistently explained by any combination of remnant lens

and main-sequence companion. This analysis would depend critically on the values of the measurements, so we do not explore it further here. We simply note that this scenario could also be strongly constrained by future astrometry.

5. Discussion

With the measurements presented here, and the precision with which these measurements allow us to determine the properties of the planet OGLE-2005-BLG-071Lb and its host, it is now possible to place this system in the context of similar planetary systems discovered by radial velocity (RV) surveys. Of course, the kind of information that can be inferred about the planetary systems discovered via RV differs somewhat from that presented here. For example, for planets discovered via RV, it is generally only possible to infer a lower limit to the planet mass, unless the planets happen to transit or produce a detectable astrometric signal. *Mutatis mutandis*, for planets discovered via microlensing, it is generally only possible to measure the projected separation at the time of the event, even in the case for which the microlensing mass degeneracy is broken as it is here (although see Gaudi et al. 2008).

With these caveats in mind, we can compare the properties of OGLE-2005-BLG-071Lb and its host star with similar RV systems. It is interesting to note that the fractional uncertainties in the host mass and distance of OGLE-2005-BLG-071Lb are comparable to those of some of the systems listed in Table 3. This clearly and quantitatively demonstrates that it is possible to acquire comparably detailed information about the host stars of planetary microlensing events, albeit using radically different kinds of information.

OGLE-2005-BLG-071Lb is one of only seven Jovian-mass planets ($0.2M_{\rm Jupiter} < M_p < 13M_{\rm Jupiter}$) that have been detected orbiting M dwarf hosts (i.e., $M_* < 0.55\ M_\odot$) (Marcy et al. 1998, 2001; Butler et al. 2006; Johnson et al. 2007b). Table 3 summarizes the planetary and host-star properties of the known M dwarf/Jovian-mass planetary systems. OGLE-2005-BLG-071Lb is likely the most massive known planet orbiting an M dwarf, and, assuming the wide solution is correct, it is also likely the most distant from its host star.

As suggested by the small number of systems listed in Table 3, and shown quantitatively by several recent studies, the frequency of relatively short period $P \lesssim 2000$ days, Jupiter-mass companions to M dwarfs appears to be $\sim 3-5$ times lower than such companions to FGK dwarfs (Butler et al. 2006; Endl et al. 2006; Johnson et al. 2007b; Cumming et al. 2008). This paucity, which has been shown to be statistically significant, is expected in the core-accretion model of planet formation, which generally predicts that Jovian companions

to M dwarfs should be rare, since for lower mass stars, the dynamical time at the sites of planet formation is longer, whereas the amount of raw material available for planet formation is smaller (Laughlin et al. 2004; Ida & Lin 2005; Kennedy & Kenyon 2008, but see Kornet et al. 2006). Thus, these planets typically do not reach sufficient mass to accrete a massive gaseous envelope over the lifetime of the disk. Consequently, such models also predict that in the outer regions of their planetary systems, lower-mass stars should host a much larger population of 'failed Jupiters,' cores of mass $\lesssim 10\ M_\oplus$ (Laughlin et al. 2004; Ida & Lin 2005). Such a population was indeed identified based on two microlensing planet discoveries (Beaulieu et al. 2006; Gould et al. 2006).

Our detection of a $\sim 3\,M_{\rm Jupiter}$ companion to an M dwarf may therefore present a difficulty for the core-accretion scenario. While we do not have a constraint on the metallicity of the host, the fact that it is likely a member of the thick disk suggests that its metallicity may be subsolar. If so, this would pose an additional difficulty for the core-accretion scenario, which also predicts that massive planets should be rarer around metal-poor stars (Ida & Lin 2004), as has been demonstrated observationally (Santos et al. 2004; Fischer & Valenti 2005). This might imply that a different mechanism is responsible for planet formation in the OGLE-2005-BLG-071L system, such as the gravitational instability mechanism (Boss 2002, 2006).

One way to escape these potential difficulties is if the host lens is actually a stellar remnant, such as white dwarf. The progenitors of remnants are generally more massive stars, which are both predicted (Ida & Lin 2005; Kennedy & Kenyon 2008) and observed (Johnson et al. 2007a,b) to have a higher incidence of massive planets. As we discussed above, future astrometric measurements could constrain both the low-metallicity and remnant-lens hypotheses. These measurements are therefore critical.

Although it is difficult to draw robust conclusions from a single system, there are now four published detections of Jovian-mass planetary companions with microlensing (Bond et al. 2004; Gaudi et al. 2008), and several additional such planets have been detected that are currently being analyzed. It is therefore reasonable to expect several detections per year (Gould 2008), and thus that it will soon be possible to use microlensing to constrain the frequency of massive planetary companions. These constraints are complementary to those from RV, since the microlensing detection method is less biased with respect to host star mass (Gould 2000), and furthermore probes a different region of parameter space, namely cool planets beyond the snow line with equilibrium temperatures similar to the giant planets in our solar system (see, e.g. Gould et al. 2007 and Gould 2008).

We thank Marc Pinsonneault and Deokkeun An for providing us their unpublished

isochrones. S.D. wishes to thank David Will of Ohio State astronomy department for setting up and maintaining the Condor system, which greatly facilitates the computations for this work. S.D. is grateful to Ondrej Pejcha and David Heyrovsky for interesting discussions on limb-darkening. Based on observations with the NASA/ESA Hubble Space Telescope obtained at the Space Telescope Science Institute, which is operated by the Association of Universities for Research in Astronomy, Incorporated, under NASA contract NAS5-26555. Support for this work was provided by NASA through grant HST-GO-10707.01-A from STScI. S.D. and A.G. were supported in part by grant AST 042758 from the NSF. S.D., A.G., D.D. and R.P. acknowledge support by NASA grant NNG04GL51G. Support for OGLE project was provided by Polish MNiSW grant N20303032/4275. B.G.P. was supported by the grant (KRF-2006-311-C00072) from Korea Research Foundation. HC was supported by the Science Research Center from Korea Science and Engineering Foundation. The MOA project is supported by Ministry of Education, Culture, Sports, Science and Technology (MEXT) of Japan, Grant-in-Aid for Specially Promoted Research No. 14002006. JPB, PF, AC, CC, SB, JBM acknowledge the financial support of ANR HOLMES. KHC's work performed under the auspices of the U.S. Department of Energy by Lawrence Livermore National Laboratory under Contract DE-AC52-07NA27344. This work was supported in part by an allocation of computing time from the Ohio Supercomputer Center.

A. Extracting Orbital Parameters for Circular Planetary Orbit

OGLE-2005-BLG-071 is the first planetary microlensing event for which the effects of planetary orbital motion in the light curve has been been fully analyzed. The distortions of the light curve due to the orbital motion are modeled by ω and $\dot{b}$ as discussed in § 3.2. In addition, the lens mass M and distance D_l are determined, so we can directly convert the microlens light-curve parameters that are normalized to the Einstein radius to physical parameters. In this section, we show that under the assumption of a circular planetary orbit, the planetary orbital parameters can be deduced from the light-curve parameters. Let $r_\perp = D_l \theta_{\rm E} b$ be the projected star-planet separation and let $r_\perp \boldsymbol{\gamma}$ be the instantaneous planet velocity in the plane of the sky, i.e. $r_\perp \gamma_\perp = r_\perp \omega$ is the velocity perpendicular to this axis and $r_\perp \gamma_\parallel = r_\perp \dot{b}/b$ is the velocity parallel to this axis. Let a be the semi-major axis and define the $\hat{\boldsymbol{\imath}}$, $\hat{\boldsymbol{\jmath}}$, $\hat{\boldsymbol{k}}$ directions as the instantaneous star-planet-axis on the sky plane, the direction into the sky, and $\hat{\boldsymbol{k}} = \hat{\boldsymbol{\imath}} \times \hat{\boldsymbol{\jmath}}$. Then the instantaneous velocity of the planet is

$$\mathbf{v} = \sqrt{\frac{GM}{a}} [\cos\theta \hat{\boldsymbol{k}} + \sin\theta (\cos\phi \hat{\boldsymbol{\imath}} - \sin\phi \hat{\boldsymbol{\jmath}})], \tag{A1}$$

where ϕ is the angle between star-planet-observer (i.e., $r_\perp = a \sin\phi$) and θ is the angle of the velocity relative to the $\hat{\boldsymbol{k}}$ direction on the plane that is perpendicular to the planet-star-axis.

We thus obtain

$$\gamma_\perp = \sqrt{\frac{GM}{a^3}}\frac{\cos\theta}{\sin\phi}, \qquad \gamma_\parallel = \sqrt{\frac{GM}{a^3}}\sin\theta\cot\phi. \tag{A2}$$

To facilitate the derivation, we define

$$A \equiv \frac{\gamma_\parallel}{\gamma_\perp} = -\tan\theta\cos\phi, \qquad B \equiv \frac{r_\perp^3\gamma_\perp^2}{GM} = \cos^2\theta\sin\phi, \tag{A3}$$

which yield as an equation for $\sin\phi$:

$$B = F(\sin\phi); \qquad F(x) = \frac{x(1-x^2)}{A^2+1-x^2}. \tag{A4}$$

Note that $F'(\sin\phi) = 0$ when $\sin^2\phi_* = (3/2)A^2 + 1 - |A|\sqrt{(9/4)A^2+2}$. So equation (A4) has two degenerate solutions when $B < F(\sin\phi_*)$ and has no solutions when $B > F(\sin\phi_*)$. Subsequently, one obtains,

$$a = \frac{r_\perp}{\sin\phi}, \qquad \cos i = -\sin\phi\cos\theta, \qquad K = \sqrt{\frac{GM}{a}}q\sin i, \tag{A5}$$

where i is the inclination and K is the amplitude of radial velocity.

The Jacobian matrix used to transform from $P(r_\perp, \gamma_\perp, \gamma_\parallel)$ to $P(a, \phi, \theta)$ is given below,

$$\begin{aligned}\frac{\partial(r_\perp,\gamma_\perp,\gamma_\parallel)}{\partial(a,\phi,\theta)} &= \frac{GM}{a^3}\begin{vmatrix} \sin\phi & a\cos\phi & 0 \\ -\frac{3}{2a}\frac{\cos\theta}{\sin\phi} & -\frac{\cos\theta\cos\phi}{\sin^2\phi} & -\frac{\sin\theta}{\sin\phi} \\ -\frac{3}{2a}\sin\theta\cot\phi & -\frac{\sin\theta}{\sin^2\phi} & \cos\theta\cot\phi \end{vmatrix} \\ &= \frac{GM}{a^3}\cot^2\phi\Big(\frac{1}{2} - \sin^2\theta\tan^2\phi\Big).\end{aligned} \tag{A6}$$

Then for an arbitrary function $H(a)$,

$$\frac{\partial(r_\perp,\gamma_\perp,\gamma_\parallel)}{\partial(H(a),\cos\phi,\theta)} = \frac{\partial(r_\perp,\gamma_\perp,\gamma_\parallel)}{\partial(a,\phi,\theta)} \times \frac{1}{\sin\phi H'(a)}, \tag{A7}$$

which, for the special case of a flat distribution, $H(a) = \ln a$, yields,

$$\frac{\partial(r_\perp,\gamma_\perp,\gamma_\parallel)}{\partial(ln(a),\cos\phi,\theta)} = \frac{GM}{r_\perp^2}\frac{\cos^2\phi}{\sin\phi}.\Big(\frac{1}{2} - \sin^2\theta\tan^2\phi\Big) \tag{A8}$$

REFERENCES

Albrow, M. D., et al. 1999, ApJ, 512, 672

An, J. H., et al. 2002, ApJ, 572, 521

An, J. H. 2005, MNRAS, 356, 1409

Anderson, J. & King, I. R. 2004, Hubble Space Telescope Advanced Camera for Surveys Instrument Science Report 04-15

Bean, J. L., Benedict, G. F., & Endl, M. 2006, ApJ, 653, L65

Beaulieu, J.-P., et al. 2006, Nature, 439, 437

Benedict, G. F., et al. 2002, ApJ, 581, L115

Bennett, D. P., Anderson, J., Bond, I. A., Udalski, A., & Gould, A. 2006, ApJ, 647, L171

Bennett, D. P., Anderson, J., & Gaudi, B. S. 2007, ApJ, 660, 781

Bessell, M. S., & Brett, J. M. 1988, PASP, 100, 1134

Bond, I. A., et al. 2004, ApJ, 606, L155

Boss, A. P. 2002, ApJ, 567, L149

Boss, A. P. 2006, ApJ, 643, 501

Butler, R. P., Johnson, J. A., Marcy, G. W., Wright, J. T., Vogt, S. S., & Fischer, D. A. 2006, PASP, 118, 1685

Chang, K., & Refsdal, S. 1979, Nature, 282, 561

Claret, A. 2000, A&A, 363, 8081

Cumming, A., Butler, R. P., Marcy, G. W., Vogt, S. S., Wright, J. T., & Fischer, D. A. 2008, PASP, in press (arXiv:0803.3357)

Delfosse, X., Forveille, T., Mayor, M., Perrier, C., Naef, D., & Queloz, D. 1998, A&A, 338, L67

Dong, S., et al. 2006, ApJ, 642, 842

Doran, M., & Mueller, C. M. 2004, J. Cosmology Astropart. Phys., JCAP09(2004)003

Duquennoy, A., & Mayor, M. 1991, A&A, 248, 485

Dominik, M. 1999, A&A, 349, 108

Einstein, A. 1936, Science, 84, 506

Endl, M., Cochran, W. D., Kürster, M., Paulson, D. B., Wittenmyer, R. A., MacQueen, P. J., & Tull, R. G. 2006, ApJ, 649, 436

Fischer, D. A., & Valenti, J. 2005, ApJ, 622, 1102

Gaudi, B. S. 2007, "Extreme Solar Systems," ASP Conference Series, ed. Debra Fischer, Fred Rasio, Steve Thorsett and Alex Wolszczan (arXiv:0711.1614)

Gaudi, B. S., et al. 2008, Science, 319, 927

Gould, A. 1992, ApJ, 392, 442

Gould, A. 1994, ApJ, 421, l71

Gould, A. 2000, ApJ, 535, 928

Gould, A. 2004, ApJ, 606, 319

Gould, A. 2008, ApJ, accepted, (arXiv:0801.2578)

Gould, A. 2008, to appear in The Variable Universe: A Celebration of Bohdan Paczynski, (arXiv:0803.4324)

Gould, A., Miralda-Escude, J., & Bahcall, J. N. 1994, ApJ, 423, L105

Gould, A. et al. 2006, ApJ, 644, L37

Gould, A., Gaudi, B. S., & Bennett, D. P. 2007, preprint (arXiv:0704.0767)

Kervella, P., Thévenin, F., Di Folco, E., & Ségransan, D. 2004, A&A, 426, 297

Kozłowski, S., Woźniak, P. R., Mao, S., & Wood, A. 2007, ApJ, 671, 420

Kubas, D., et al. 2008, A&A, in press, (arXiv:0710.5306)

Ida, S., & Lin, D. N. C. 2004, ApJ, 616, 567

Ida, S., & Lin, D. N. C. 2005, ApJ, 626, 1045

Johnson, J. A., et al. 2007a, ApJ, 665, 785

Johnson, J. A., Butler, R. P., Marcy, G. W., Fischer, D. A., Vogt, S. S., Wright, J. T., & Peek, K. M. G. 2007b, ApJ, 670, 833

Kennedy, G. M., & Kenyon, S. J. 2008, ApJ, 673, 502

Kornet, K., Wolf, S., & Różyczka, M. 2006, A&A, 458, 661

Laughlin, G., Bodenheimer, P., & Adams, F. C. 2004, ApJ, 612, L73

Lejeune, T., Cuisinier, F., & Buser, R. 1997, A&AS, 125, 229

Lejeune, T., Cuisinier, F., & Buser, R. 1998, A&AS, 130, 65

Manfroid, J. 1995, A&AS, 113, 587

Marcy, G. W., Butler, R. P., Vogt, S. S., Fischer, D., & Lissauer, J. J. 1998, ApJ, 505, L147

Marcy, G. W., Butler, R. P., Fischer, D., Vogt, S. S., Lissauer, J. J., & Rivera, E. J. 2001, ApJ, 556, 296

Nishiyama, S., et al. 2005, ApJ, 621, L105

Poindexter, S. et al. 2005, ApJ, 633, 914

Rivera, E. J., et al. 2005, ApJ, 634, 625

Santos, N. C., Israelian, G., & Mayor, M. 2004, A&A, 415, 1153

Smith, M. C., Mao, S., & Paczyński, B. 2003, MNRAS, 339, 925

Udalski, A. et al. 2005, ApJ, 628, L109 (Paper I)

van Belle, G. T. 1999, PASP, 111, 1515

Wozniak, P. R. 2000, Acta Astronomica, 50, 421

Yoo, J., et al. 2004, ApJ, 603, 139

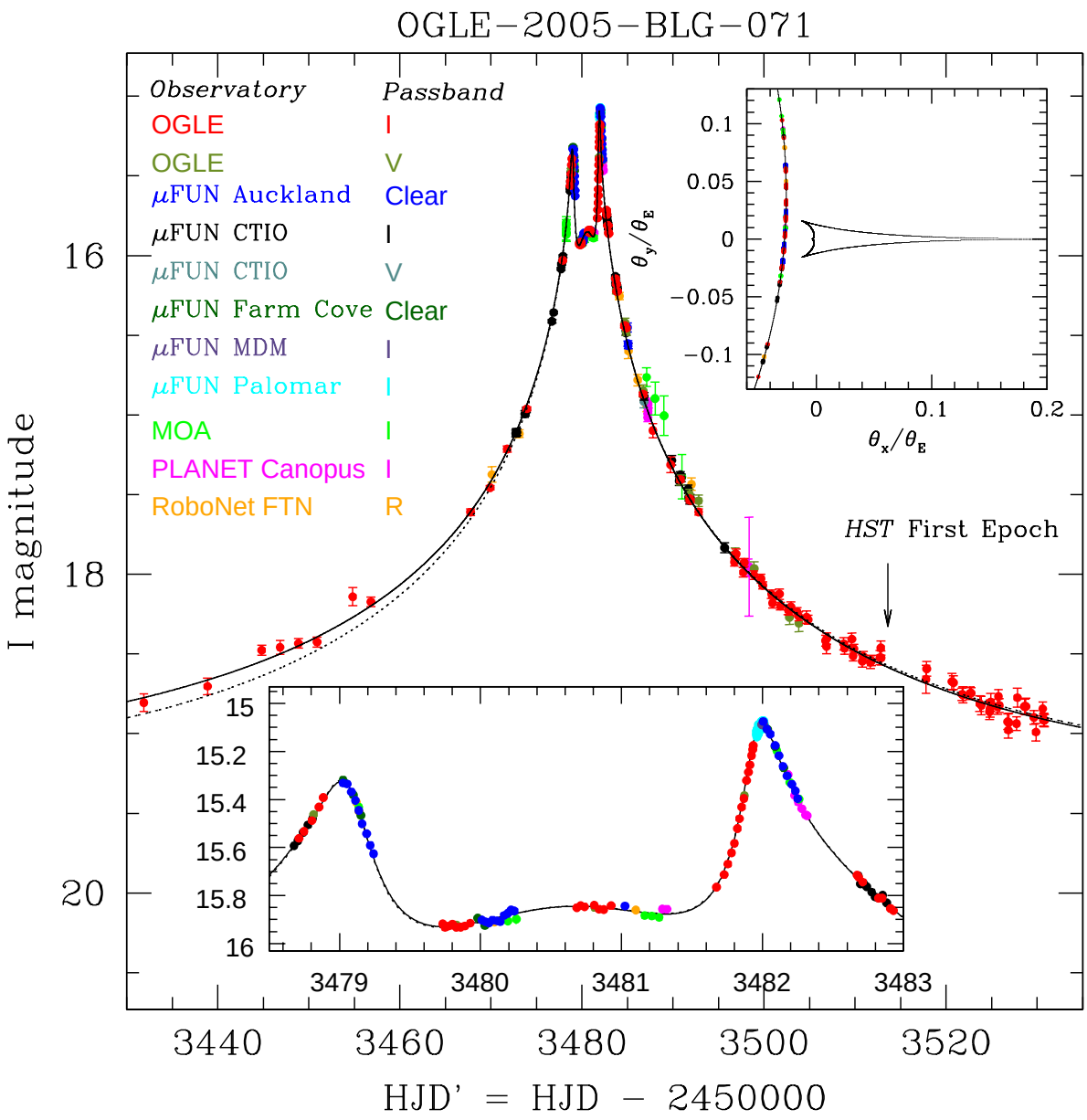

Fig. 1.— Main panel: All available ground-based data of microlensing event OGLE-2005-BLG-071. *HST* ACS HRC observations in F814W and F555W were taken at two epochs, once when the source was magnified by $A \sim 2$ (*arrow*), and again at HJD = 2453788.2 (at baseline). Planetary models that include (*solid*) and excludes (*dotted*) microlens parallax are shown. Zoom at bottom: Triple-peak feature that reveals the presence of the planet. Each of the three peaks corresponds to the source passing by a cusp of the central caustic induced by the planet. Upper inset: Trajectory of the source relative to the lens system in the units of angular Einstein radius $\theta_{\rm E}$. The lens star is at $(0, 0)$, and the star-planet axis is parallel to the x-axis. The best-fit angular size of the source star in units of $\theta_{\rm E}$ is $\rho \sim 0.0006$, too small to be resolved in this figure.

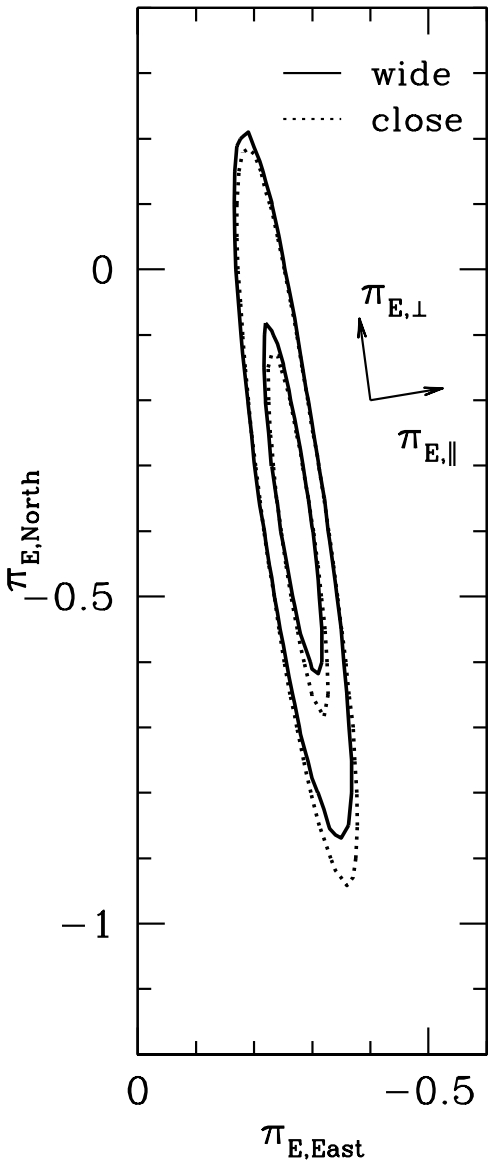

Fig. 2.— Probability contours ($\Delta\chi^2 = 1, 4$) of microlens parallax parameters derived from MCMC simulations for wide-binary (in solid line) and close-binary (in dashed line) solutions. Fig. 2 and eq. (12) in Gould (2004) imply that $\pi_{E,\perp}$ is defined so that $\pi_{E,\parallel}$ and $\pi_{E,\perp}$ form a right-handed coordinate system.

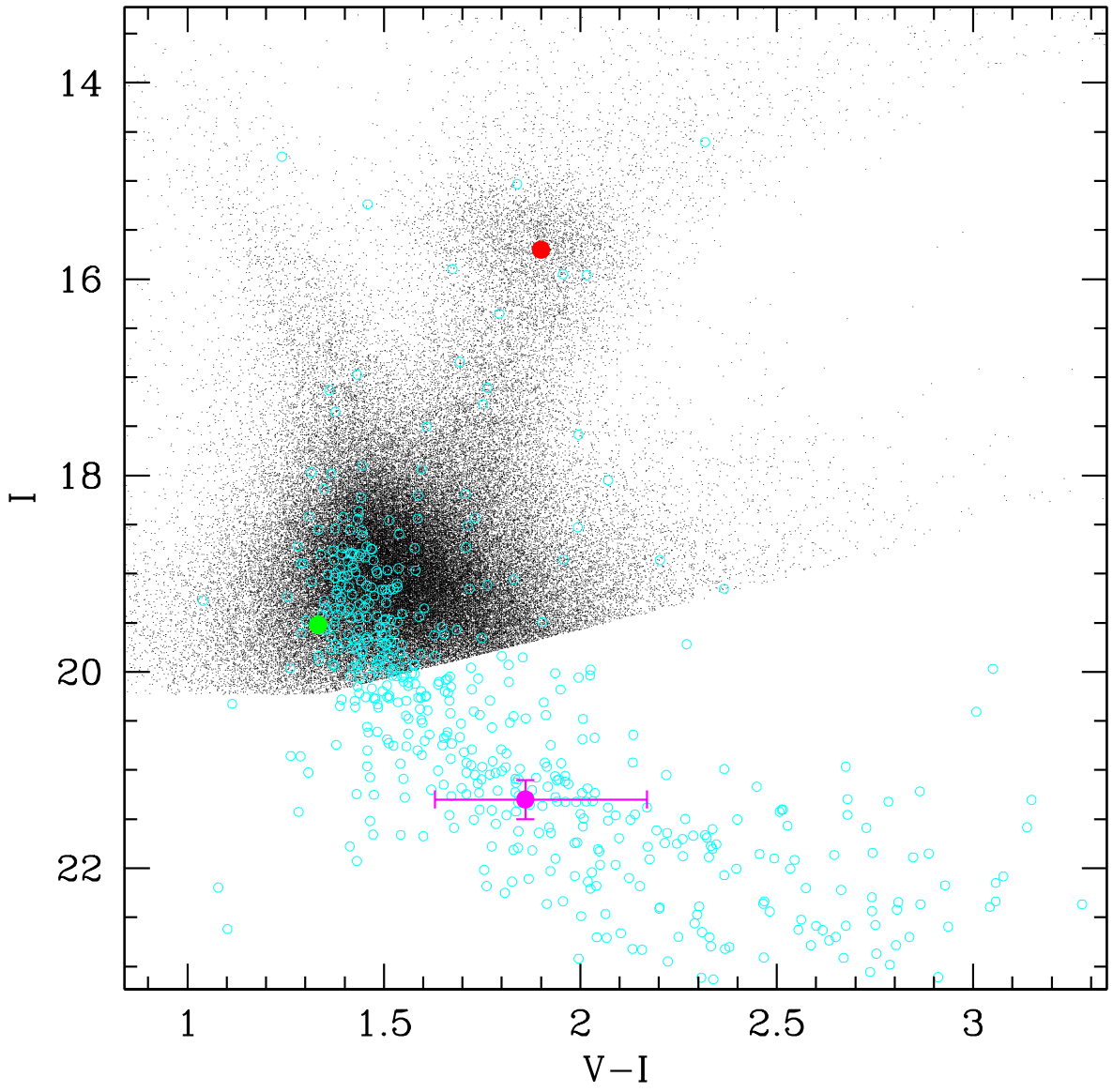

Fig. 3.— Color-Magnitude Diagram for OGLE-2005-BLG-071 field. Black dots are the stars with OGLE I-band and V-band observations. Red point and green points show the center of red clump and the source, respectively. The errors in their fluxes and colors are too small to be visible on the graph. Cyan points are the stars in the ACS field, which are photometrically aligned with OGLE stars using 10 common stars. Magenta point with error-bars show the color and magnitude of the blended light.

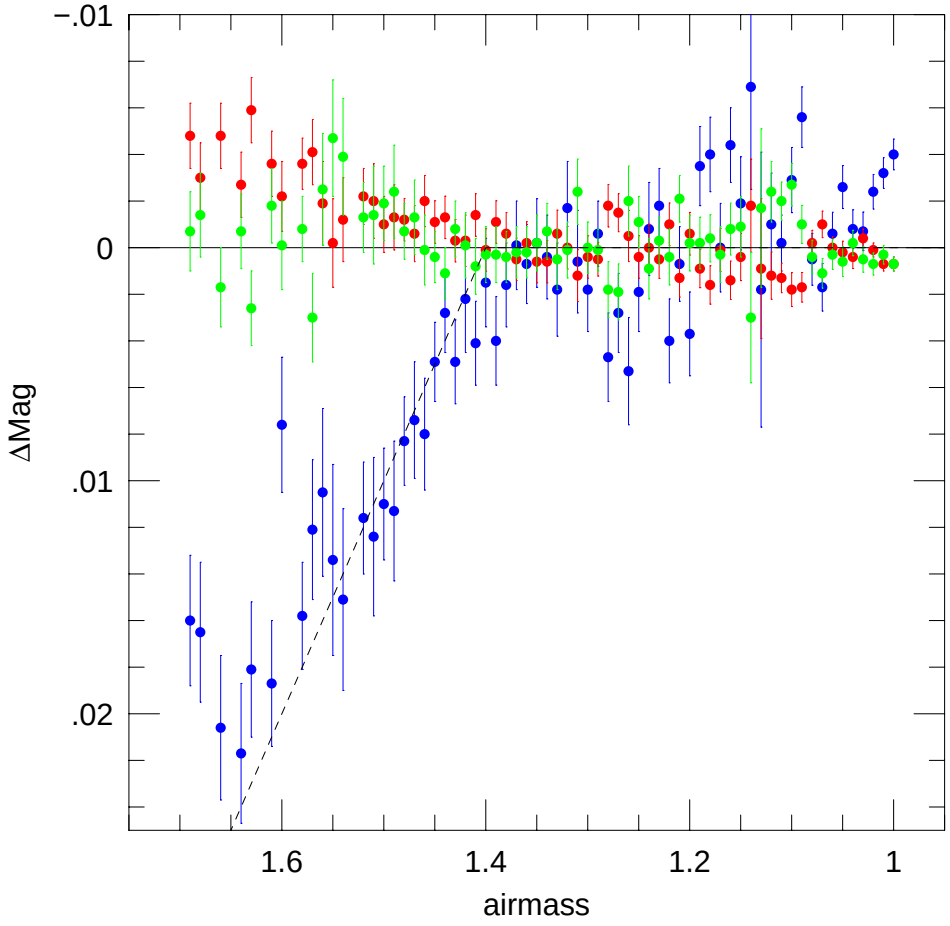

Fig. 4.— Differential extinction effects for clear-filter Auckland dataset. The flux variations are plotted as a function of airmass for bright stars ($I < 15$) in three categories: $V - I < 1.4$ (blue), $1.4 < V - I < 2.0$ (green) and $V - I > 2.0$ (red). The dashed line shows the empirical formula (eq. [9]) that we adopt to correct the source flux.

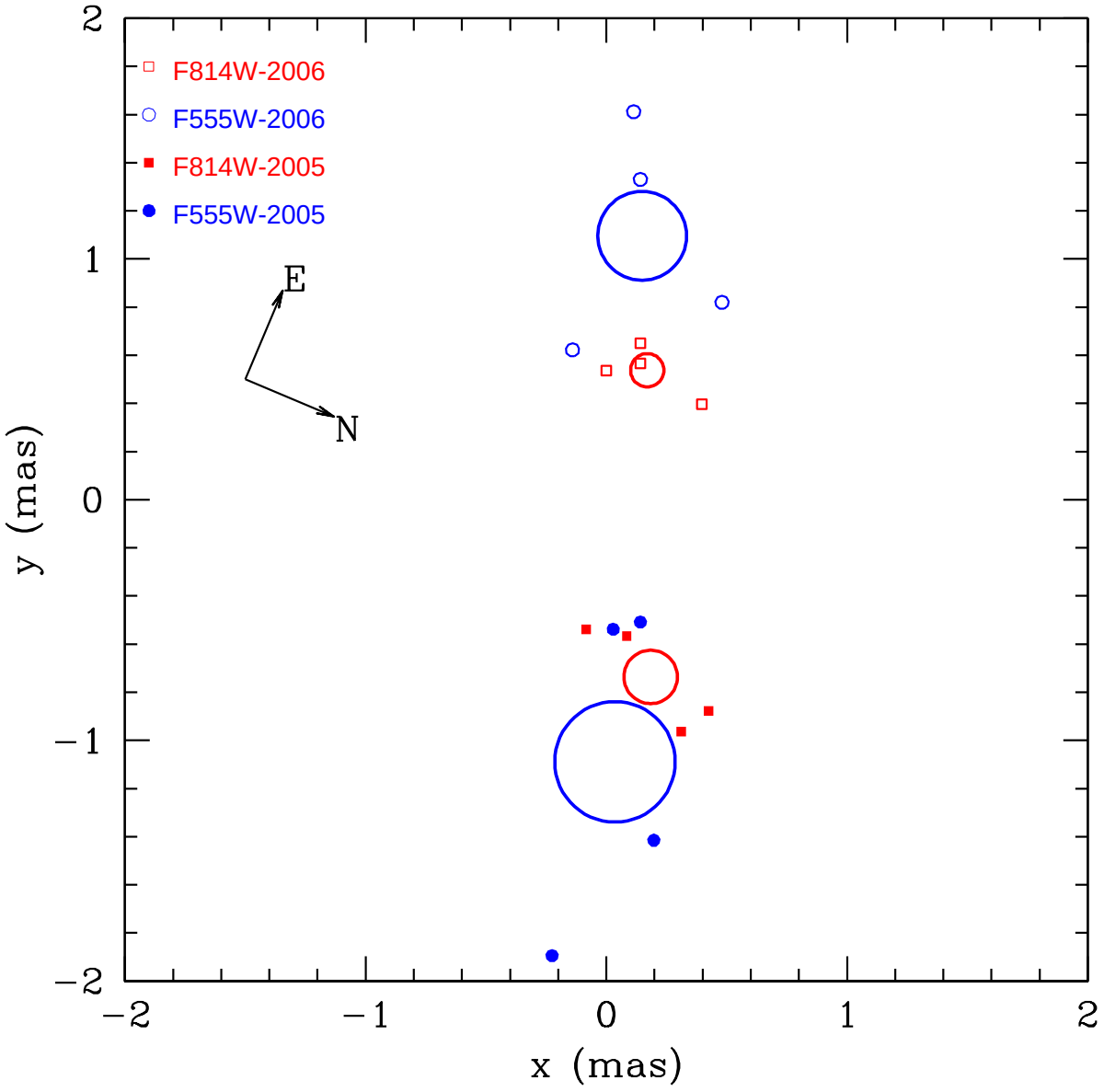

Fig. 5.— *HST* ACS astrometric measurements of the target star in F814W (red) and F555W (blue) filters in 2005 (filled dots) and 2006 (open dots). The center positions of the big circles show mean values of the 4 dithered observations in each filter at each epoch while radii of the circle represent the $1\,\sigma$ errors.

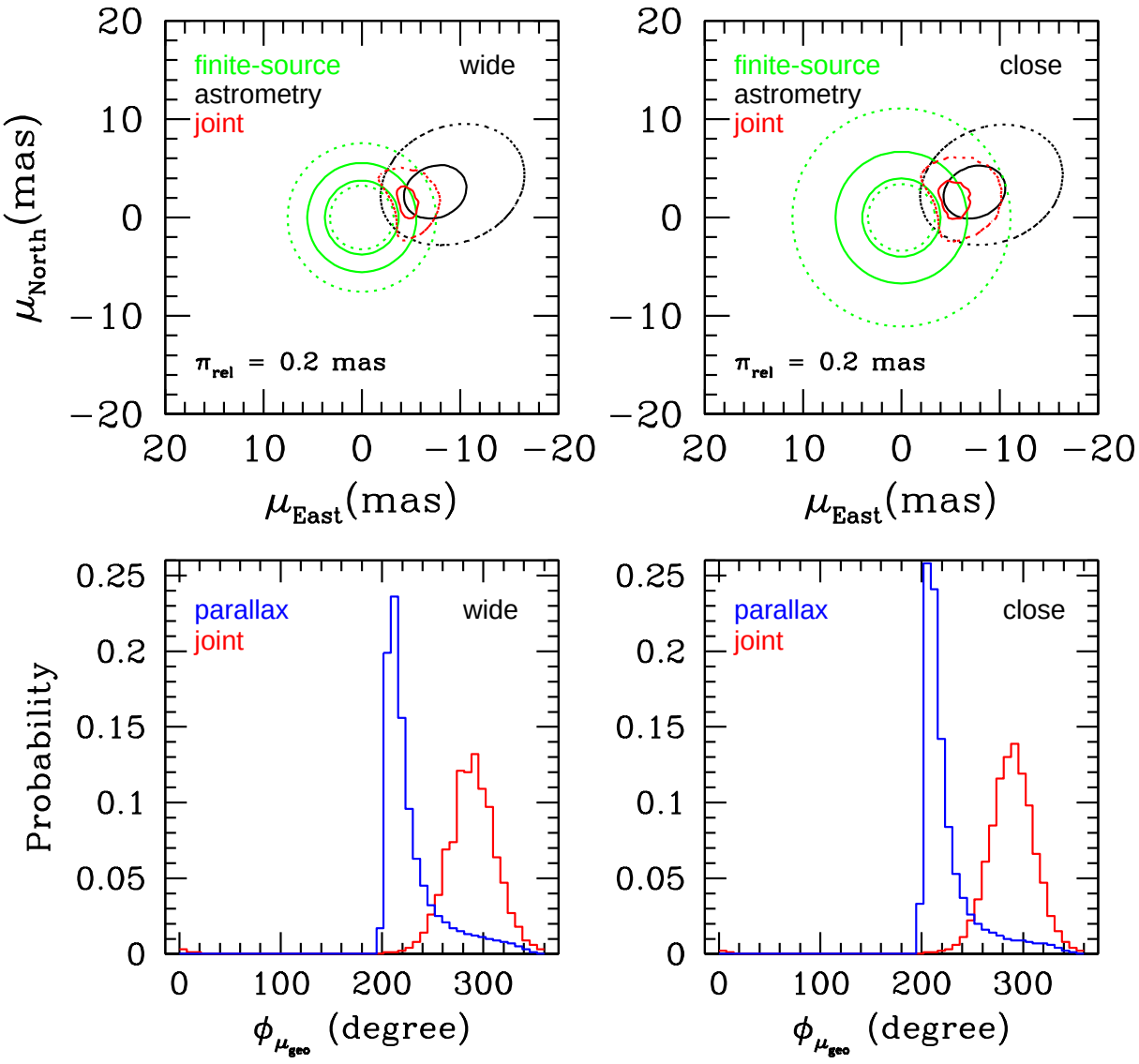

Fig. 6.— The upper two panels show posterior probability contours at $\Delta\chi^2 = 1$ (solid line) and 4 (dotted line) for relative lens-source proper motion $\boldsymbol{\mu}_{\rm geo}$. The left panel is for wide-binary solutions and the right one is for close-binary. The green contours show the probability distributions constrained by the finite-source effects. The black contours are derived from *HST* astrometry measurements assuming $\pi_{\rm rel} = 0.2\,{\rm mas}$. The red contours show the joint probability distributions from both constraints. The lower two panels show the posterior probability distribution of the position angle $\phi_{\boldsymbol{\mu}_{\rm geo}}$ of the relative lens-source proper motion for wide-binary and close-binary solutions, respectively. The histogram in red is derived from the red contours of joint probability for finite-source and astrometry constraints in the upper panel. The blue histogram represents that of the microlens parallax. They mildly disagree at 2.5σ.

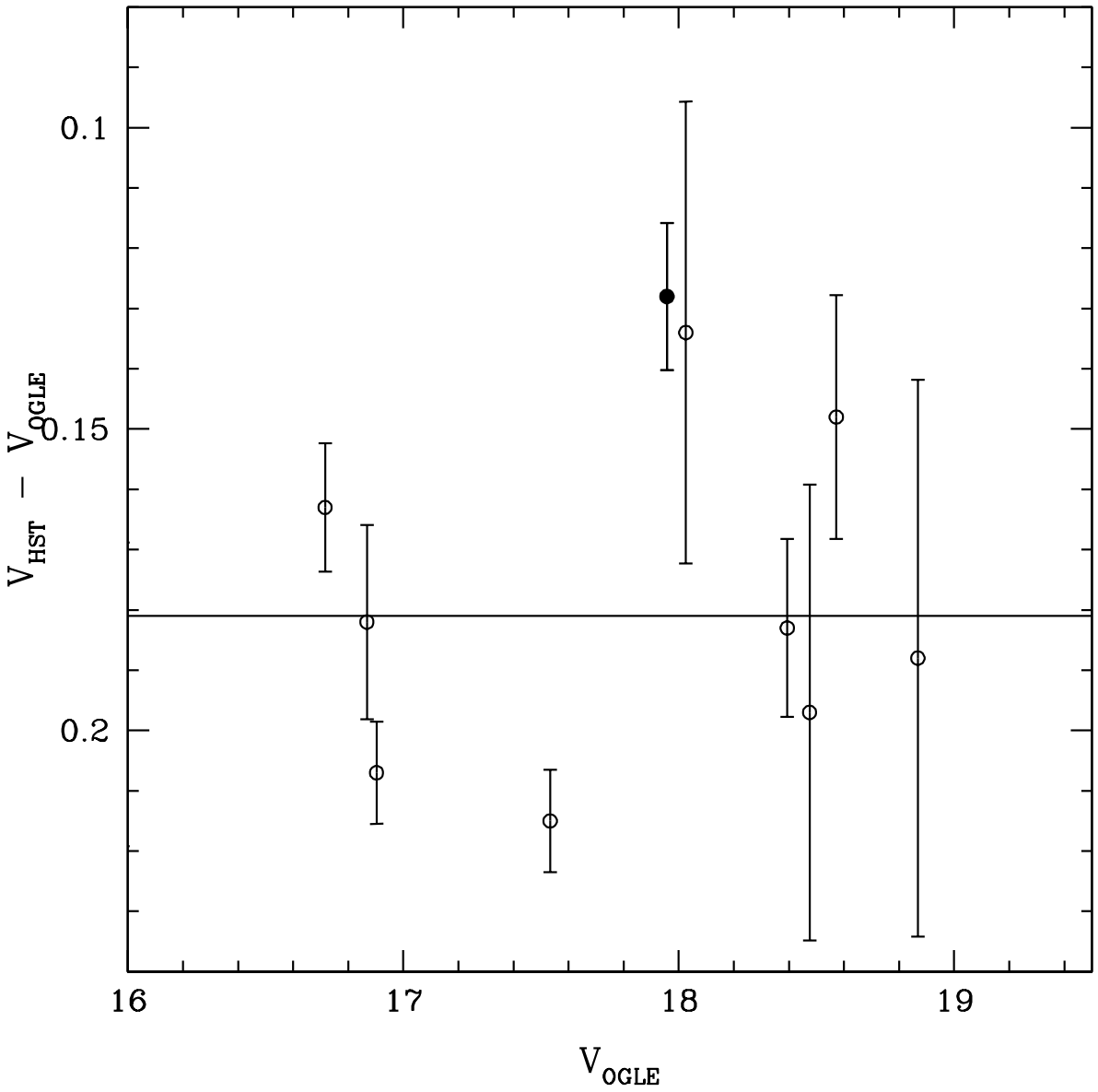

Fig. 7.— The differences between OGLE V and *HST* F555W magnitudes for the matched stars are plotted against their V magnitudes measured by OGLE. To calculate the offset, we add a 0.017 mag "cosmic error" in quadrature to each point in order to reduce χ^2/dof to unity. The open circles represent the stars used to establish the final transformation, and the filled point shows an "outlier".

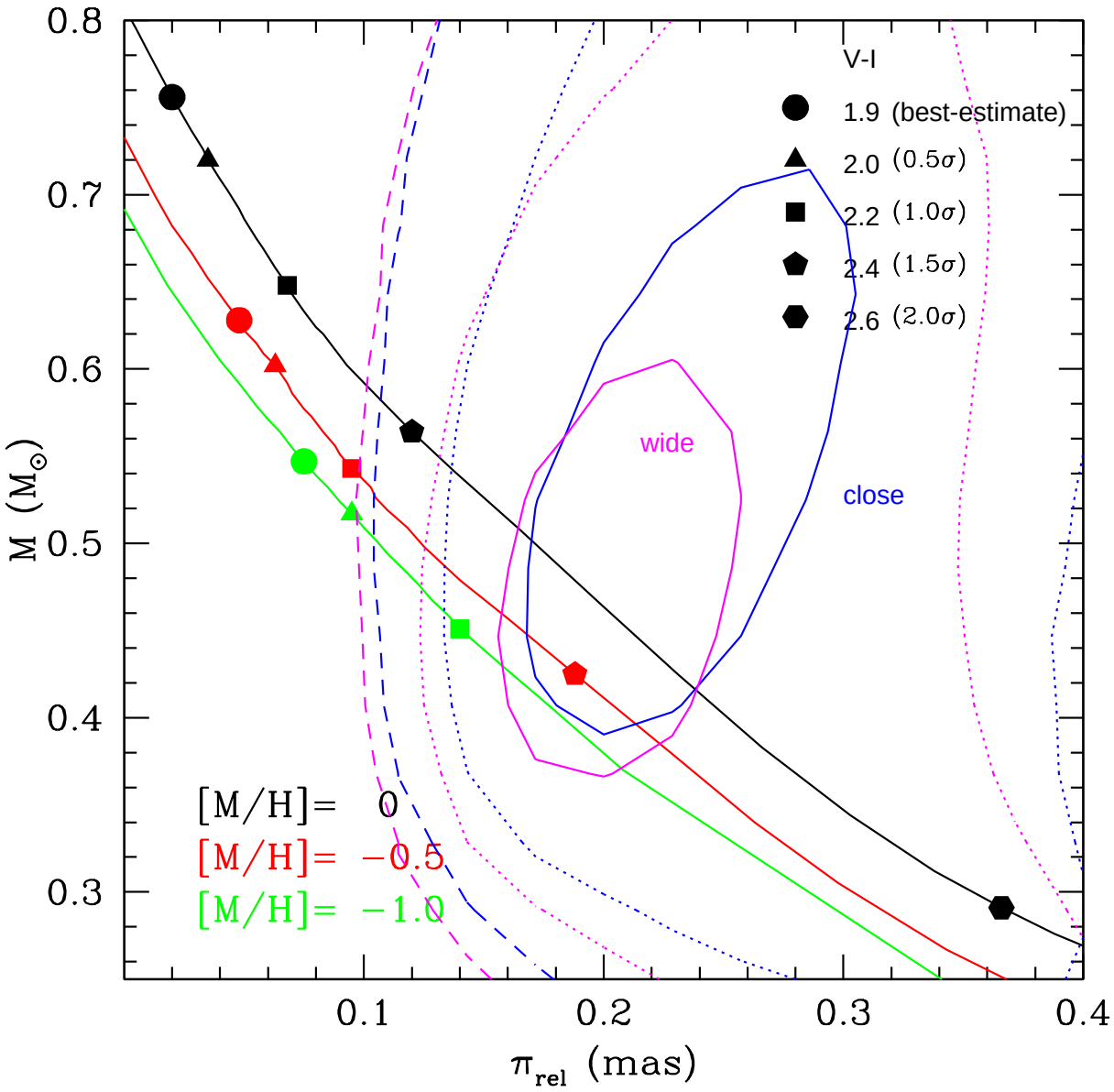

Fig. 8.— Posterior probability distribution of lens mass M and relative lens-source parallax $\pi_{\rm rel}$ from MCMC simulations discussed in § 3.6.1. The constraints include those from parallax effects, finite-source effects and relative proper motion measurements from *HST* astrometry. The $\Delta\chi^2 = 1, 4, 9$ contours are displayed in solid, dotted and dashed lines, respectively. Both wide-binary (magenta) and close-binary (blue) solutions are shown. The lines in black, red and green represent the predicted M and $\pi_{\rm rel}$ from the isochrones for different metal abundances: [M/H] = 0 (black), −0.5 (red), −1.0 (green). The points on these lines correspond to the observed I-band magnitude $I = 21.3$ and various $V - I$ values $V - I = 1.9$ (best estimate, filled dots), 2.0 ($0.5\,\sigma$, filled triangle), 2.2 ($1.0\,\sigma$, filled squares), 2.4 ($1.5\,\sigma$, filled pentagons), and 2.6 ($2.0\,\sigma$, filled hexagons)

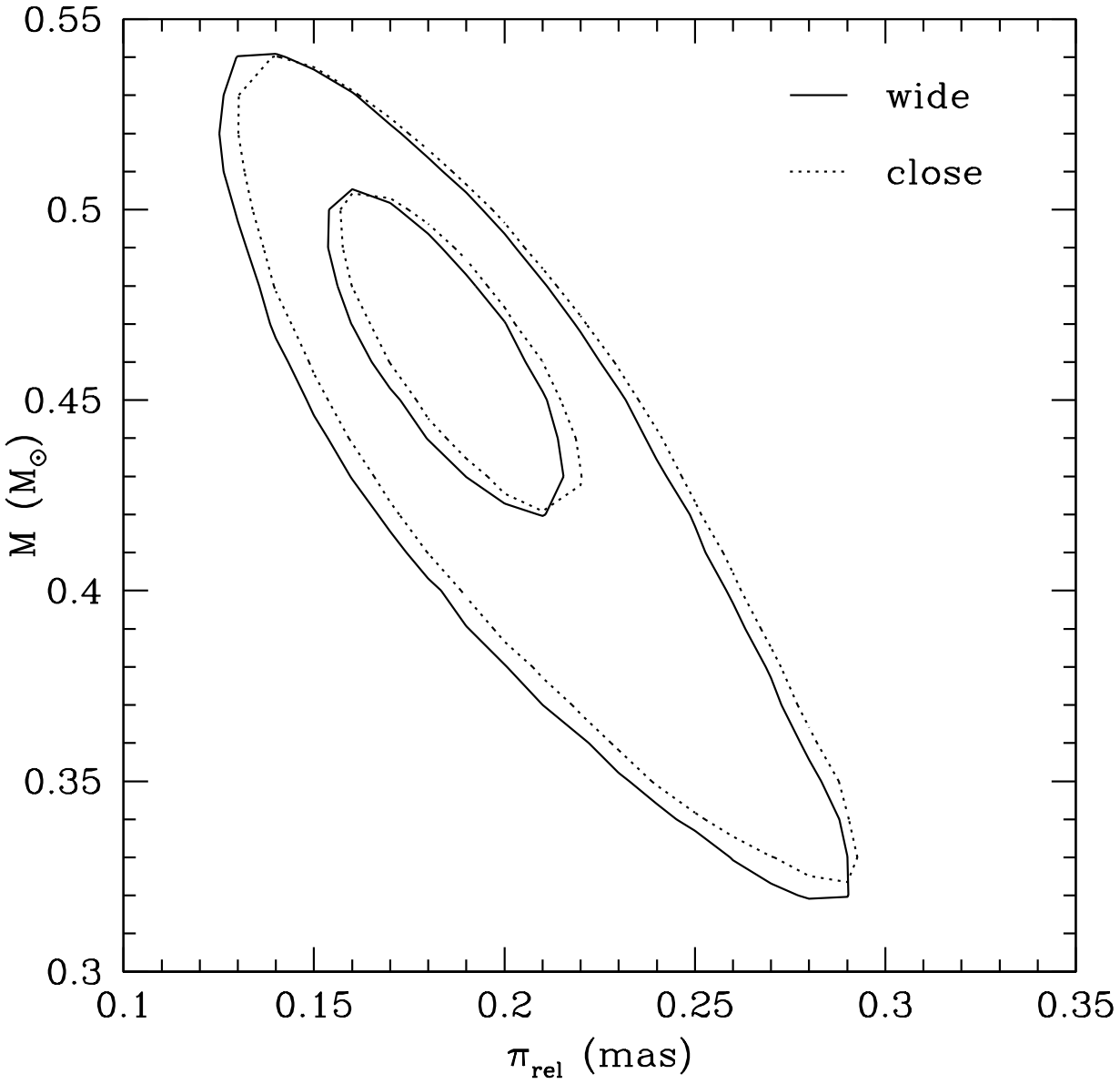

Fig. 9.— Posterior probability distribution of lens mass M and relative lens-source parallax $\pi_{\rm rel}$ from MCMC simulations assuming the blended light comes from the lens star. The $\Delta\chi^2 = 1, 4$ contours are displayed in solid line for wide solutions, and in dotted line for close solutions.

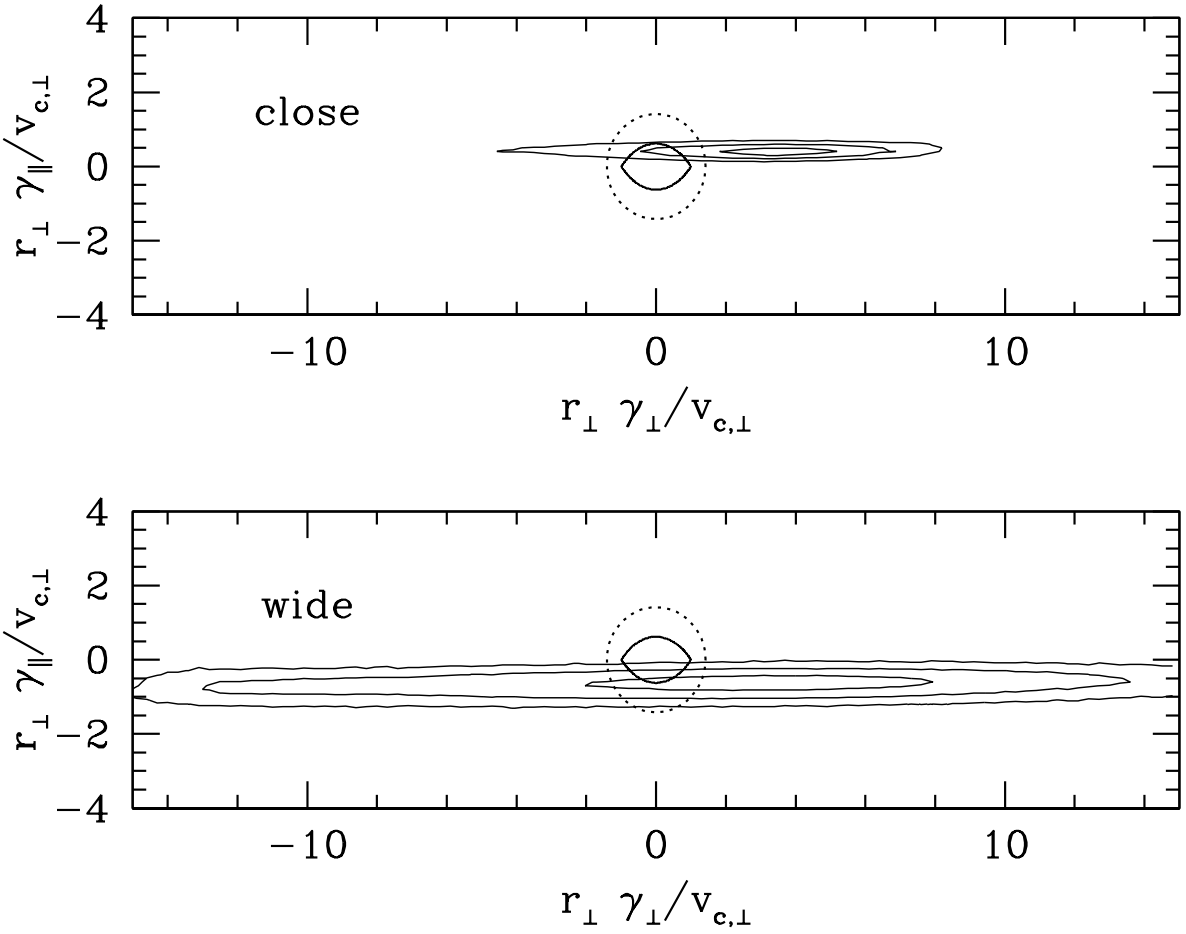

Fig. 10.— Probability contours of projected velocity $r_\perp \boldsymbol{\gamma}$ (defined in Appendix A) in the units of $v_{\mathrm{c},\perp}$ for both close-binary (upper panel) and wide-binary (lower panel) solutions. All the solutions that are outside the dotted circle are physically rejected as the velocities exceed the escape velocity of the system. The boundary in solid line inside the dotted circle encloses the solutions for which circular orbits are allowed.

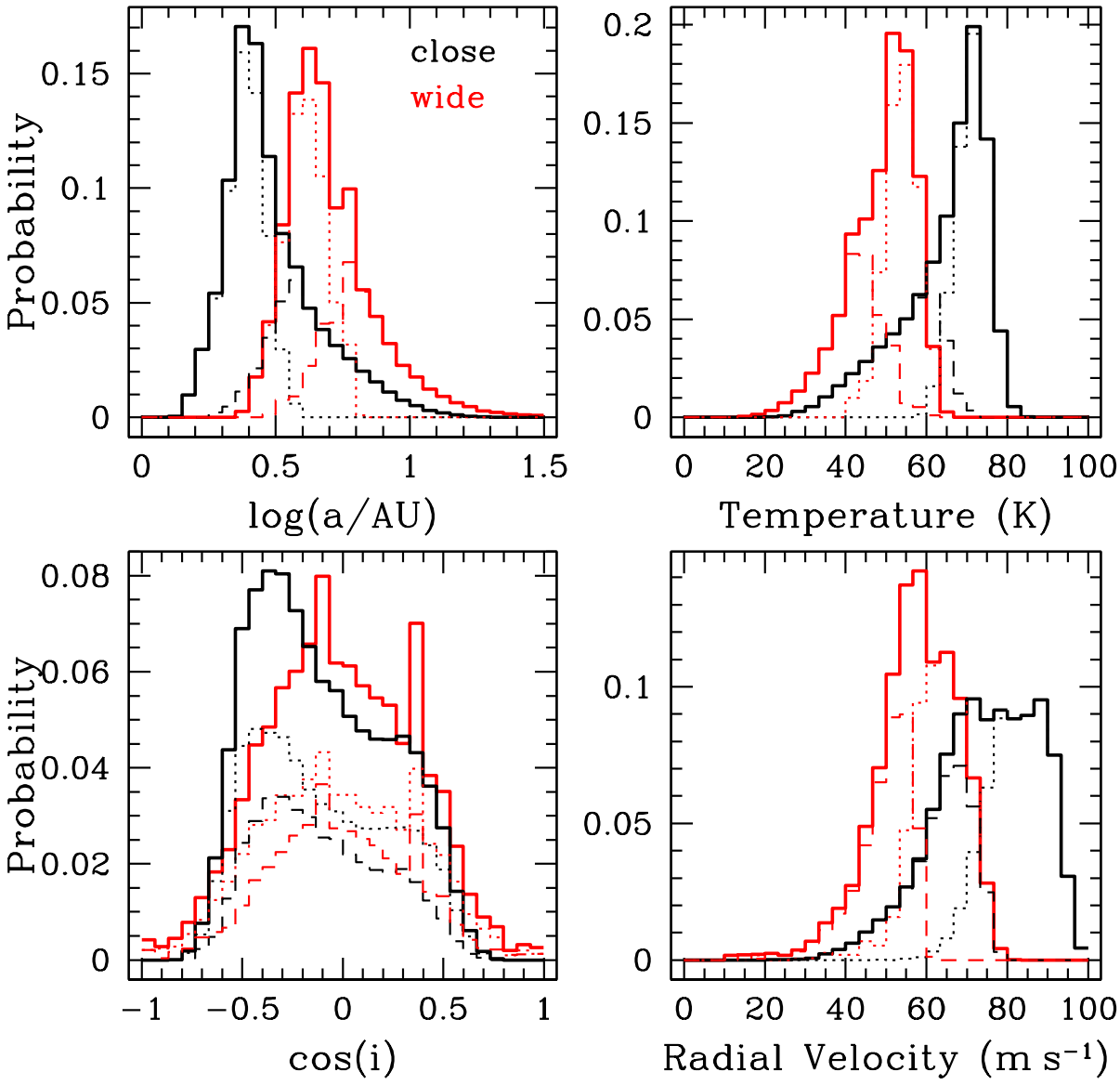

Fig. 11.— Probability distributions of planetary parameters (semi-major axis a, equilibrium temperature, cosine of the inclination, and amplitude of radial velocity of the lens star) from MCMC realizations assuming circular orbital motion. Histograms in black and red represent the close-binary and wide-binary solutions, respectively. Dotted and dashed histograms represent the two degenerate solutions for each MCMC realization discussed in Appendix A.

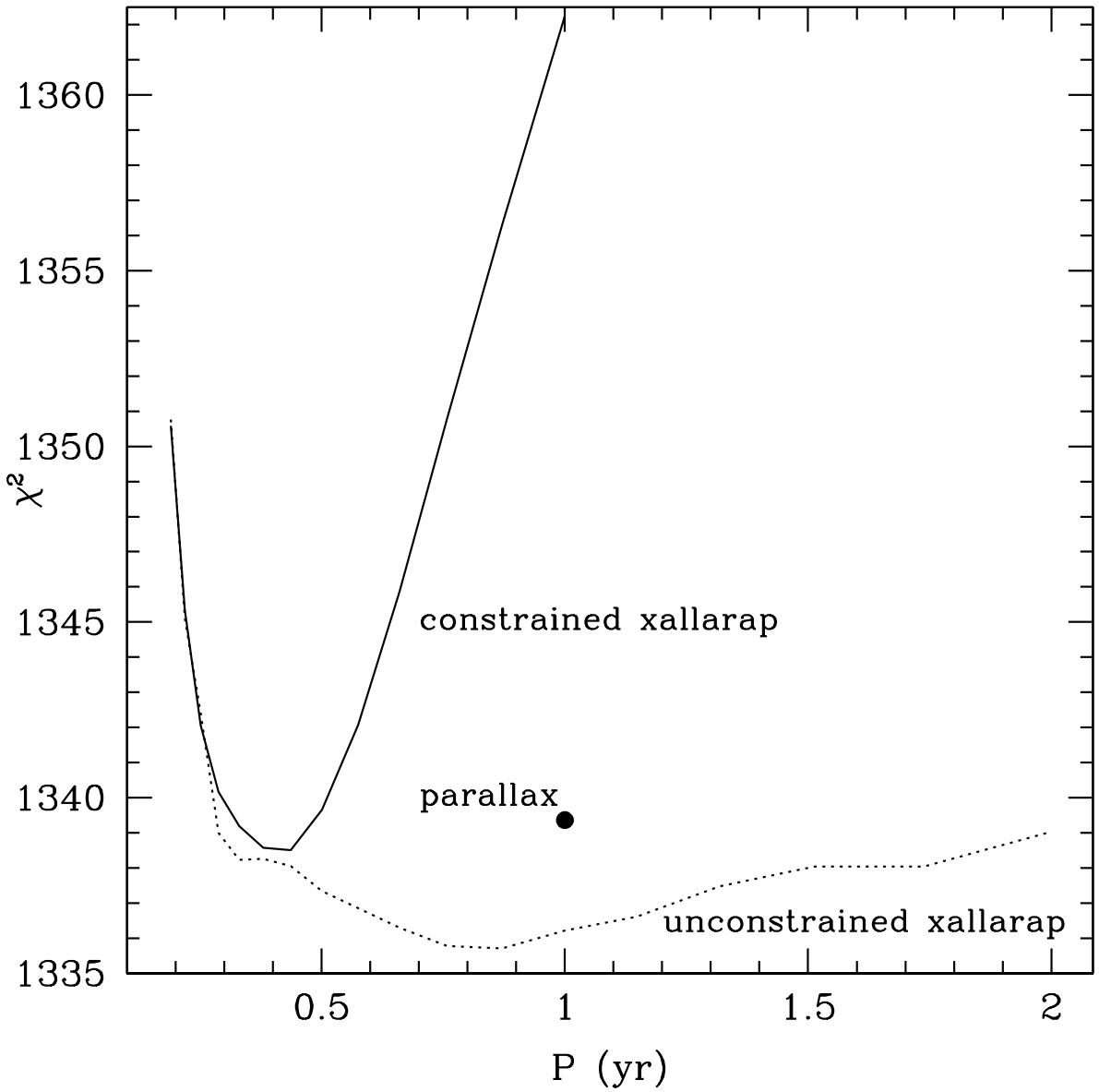

Fig. 12.— The χ^2 distributions for best-fit xallarap solutions at fixed binary-source orbital periods P. The solid and dotted lines represent xallarap fits with and without dynamical constraints described in § 3.8. The best-fit parallax solution is shown as a filled dot at period of 1 year. All of the fits shown in this figure assume no planetary orbital motion.

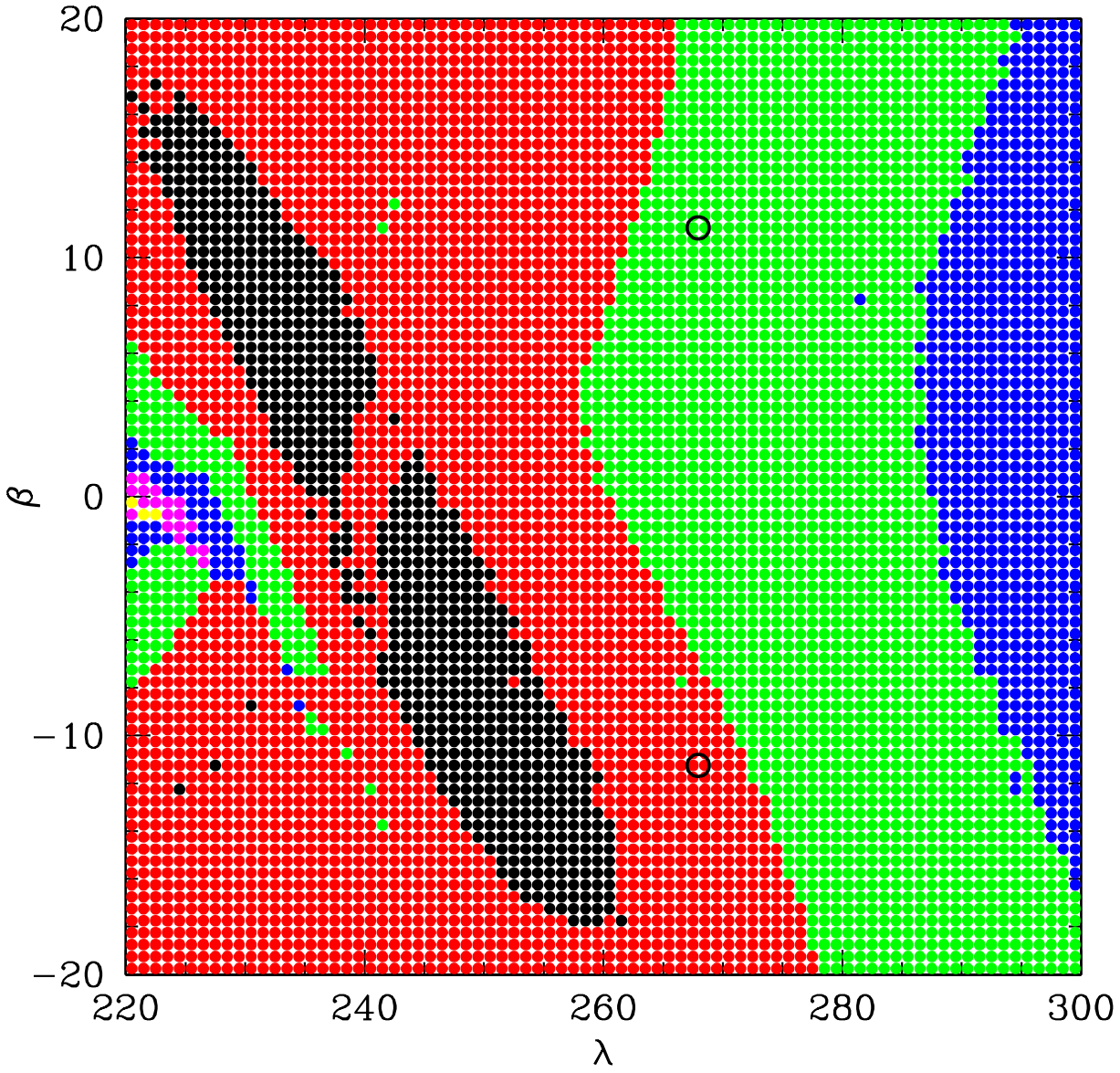

Fig. 13.— Results of xallarap fits by fixing binary orbital phase λ and complement of inclination β at period $P = 1\,\mathrm{yr}$ and $u_0 > 0$. The plot is color-coded for solutions with $\Delta\chi^2$ within 1 (black), 4 (red), 9 (green), 16 (blue), 25 (magenta), 49 (yellow) of the best-fit. The Earth parameters are indicated by black circles. Because of a perfect symmetry ($u_0 \to -u_0$ and $\alpha \to -\alpha$), the upper black circle represents Earth parameter ($\lambda = 268°$, $\beta = -11°$) for the case $u_0 < 0$. Comparison of parallax with xallarap must be made with the better of the two, i.e., the lower one.

Table 1: Light Curve Parameter Estimations From Markov chain Monte Carlo Simulations.

MCMC A

Model χ^2	t_0 (HJD')	u_0	$t_{\rm E}$ (day)	b	q $\times 10^3$	α (deg)	ρ $\times 10^4$	$\pi_{{\rm E},N}$	$\pi_{{\rm E},E}$	ω ($\rm yr^{-1}$)	$\dot{b}/b$ ($\rm yr^{-1}$)	$I_{\rm s}$ (mag)	$I_{\rm b}$ (mag)	$V_{\rm s}$ (mag)	$V_{\rm b}$ (mag)
Wide+	3480.6885	0.0277	69.4	1.283	7.0	274.26	5.5	-0.34	-0.26	0.408	-0.363	19.51	21.34	20.84	23.18
1330.3	$^{+0.0071}_{-0.0049}$	$^{+0.0009}_{-0.0010}$	$^{+2.4}_{-2.1}$	$^{+0.008}_{-0.006}$	± 0.3	$^{+0.24}_{-0.28}$	± 1.2	$^{+0.24}_{-0.25}$	± 0.05	$^{+0.539}_{-0.571}$	$^{+0.141}_{-0.122}$	± 0.03	$^{+0.21}_{-0.19}$	± 0.04	$^{+0.42}_{-0.28}$
Wide−	3480.6913	-0.0280	68.8	1.288	7.1	85.74	5.5	-0.28	-0.25	-0.365	-0.377	19.51	21.34	20.84	23.22
1330.8	$^{+0.0068}_{-0.0063}$	$^{+0.0010}_{-0.0008}$	$^{+2.3}_{-1.9}$	$^{+0.009}_{-0.008}$	± 0.4	$^{+0.28}_{-0.31}$	$^{+1.3}_{-1.4}$	$^{+0.24}_{-0.28}$	± 0.04	$^{+0.694}_{-0.558}$	$^{+0.136}_{-0.128}$	± 0.04	$^{+0.21}_{-0.19}$	± 0.04	$^{+0.40}_{-0.30}$
Close+	3480.6752	0.0239	69.2	0.766	6.7	274.41	4.5	-0.39	-0.28	0.708	0.638	19.51	21.31	20.85	23.16
1333.4	$^{+0.0044}_{-0.0050}$	$^{+0.0008}_{-0.0007}$	$^{+2.4}_{-2.2}$	± 0.002	± 0.2	$^{+0.17}_{-0.22}$	$^{+1.7}_{-1.9}$	$^{+0.25}_{-0.28}$	± 0.05	$^{+0.275}_{-0.395}$	$^{+0.117}_{-0.124}$	± 0.04	$^{+0.22}_{-0.19}$	± 0.04	$^{+0.41}_{-0.29}$
Close−	3480.6751	-0.0240	68.4	0.765	6.7	85.37	4.7	-0.39	-0.26	-1.022	0.638	19.51	21.30	20.84	23.19
1332.9	$^{+0.0043}_{-0.0051}$	± 0.0007	$^{+2.2}_{-2.1}$	± 0.003	± 0.2	± 0.23	$^{+1.5}_{-2.2}$	$^{+0.32}_{-0.23}$	± 0.05	$^{+0.442}_{-0.375}$	$^{+0.123}_{-0.118}$	± 0.03	$^{+0.23}_{-0.17}$	± 0.04	$^{+0.40}_{-0.30}$

MCMC B

Model χ^2	t_0 (HJD')	u_0	$t_{\rm E}$ (day)	b	q $\times 10^3$	α (deg)	ρ $\times 10^4$	$\pi_{{\rm E},N}$	$\pi_{{\rm E},E}$	ω ($\rm yr^{-1}$)	$\dot{b}/b$ ($\rm yr^{-1}$)	$I_{\rm s}$ (mag)	$I_{\rm b}$ (mag)	$V_{\rm s}$ (mag)	$V_{\rm b}$ (mag)
Wide+	3480.6889	0.0284	67.5	1.285	7.2	274.23	6.2	-0.01	-0.21	0.384	-0.393	19.48	21.46	20.81	24.03
1336.7	$^{+0.0062}_{-0.0055}$	± 0.0008	$^{+1.8}_{-1.4}$	$^{+0.008}_{-0.007}$	$^{+0.4}_{-0.2}$	± 0.25	± 0.5	$^{+0.09}_{-0.12}$	± 0.02	$^{+0.486}_{-0.618}$	± 0.132	± 0.03	$^{+0.22}_{-0.18}$	± 0.02	$^{+0.23}_{-0.24}$
Wide−	3480.6894	-0.0284	67.6	1.285	7.2	85.71	6.3	0.00	-0.21	-0.472	-0.391	19.48	21.43	20.81	23.97
1336.7	$^{+0.0055}_{-0.0062}$	± 0.0007	± 1.6	± 0.007	± 0.3	$^{+0.26}_{-0.24}$	± 0.4	$^{+0.10}_{-0.12}$	± 0.03	$^{+0.590}_{-0.481}$	$^{+0.131}_{-0.129}$	± 0.03	$^{+0.24}_{-0.16}$	± 0.03	$^{+0.28}_{-0.20}$
Close+	3480.6737	0.0246	67.4	0.766	6.8	274.50	6.1	-0.02	-0.21	0.888	0.670	19.49	21.44	20.82	23.95
1340.8	$^{+0.0044}_{-0.0047}$	± 0.0005	± 1.6	± 0.002	± 0.2	± 0.20	± 0.4	± 0.11	± 0.03	$^{+0.325}_{-0.412}$	$^{+0.114}_{-0.128}$	± 0.03	± 0.19	± 0.03	$^{+0.26}_{-0.20}$
Close−	3480.6745	-0.0245	67.2	0.766	6.8	85.45	6.1	0.01	-0.21	-0.946	0.675	19.49	21.40	20.82	23.98
1340.3	$^{+0.0040}_{-0.0050}$	± 0.0005	$^{+1.7}_{-1.5}$	± 0.002	± 0.2	$^{+0.21}_{-0.19}$	± 0.4	$^{+0.09}_{-0.13}$	± 0.03	$^{+0.427}_{-0.337}$	$^{+0.110}_{-0.129}$	± 0.03	$^{+0.22}_{-0.16}$	± 0.02	$^{+0.22}_{-0.23}$

Table 2: Derived Physical Parameters

Model χ^2	M $M_\odot$	$\pi_{\rm rel}$ mas	D_l kpc	$\mu_{\rm N}$ mas yr^{-1}	$\mu_{\rm E}$ mas yr^{-1}	$\theta_{\rm E}$ mas	M_p $M_{\rm Jupiter}$	$r_\perp$ AU
Wide+	0.46	0.19	3.3	-0.8	-4.3	0.84	3.5	3.6
1336.7	±0.04	±0.03	±0.4	±2.7	$^{+0.4}_{-0.2}$	±0.05	±0.3	±0.2
Wide−	0.47	0.19	3.2	-0.6	-4.3	0.84	3.5	3.6
1336.7	$^{+0.03}_{-0.05}$	±0.04	±0.4	$^{+3.1}_{-2.8}$	$^{+0.4}_{-0.2}$	±0.05	±0.3	±0.2
Close+	0.46	0.19	3.2	-0.9	-4.4	0.85	3.3	2.1
1340.8	$^{+0.04}_{-0.05}$	$^{+0.04}_{-0.03}$	±0.3	$^{+3.0}_{-2.7}$	$^{+0.4}_{-0.2}$	±0.04	±0.3	±0.1
Close−	0.46	0.19	3.2	-0.3	-4.4	0.85	3.3	2.1
1340.3	±0.04	±0.04	±0.4	$^{+2.8}_{-3.2}$	$^{+0.4}_{-0.2}$	$^{+0.04}_{-0.05}$	$^{+0.3}_{-0.4}$	±0.1

Table 3: Jovian-mass Companions to M Dwarfs ($M_* < 0.55\ M_\odot$)

Name	M_* ($M_\odot$)	Metallicity	Dist. (pc)	M_p ($M_{\rm Jup}$)	P (days)	a (AU)	Ref.
GJ 876c	0.32 ±0.03	−0.12 ±0.12	4.660 ±0.004	$0.619/\sin i$	30.340 ±0.013	0.13030	1,2,3
GJ 876b	–	–	–	1.9– 2.5	60.940 ±0.013	0.20783	–
GJ 849b	0.49 ±0.05	0.16 ±0.2	8.8 ±0.2	$0.82/\sin i$	1890 ±130	2.35	4
GJ 317b	0.24 ±0.04	−0.23 0.2	9.2 ±1.7	$1.2/\sin i$	692.9 ±4	0.95	5
OB06109Lb	0.50 ±0.05	? ?	1490 ±130	0.71 ±0.08	1830 ±370	2.3 ±0.2	6
OB06109Lc	– –	– –	– –	0.27 ±0.03	5100 ±730	4.6 ±0.5	–
OGLE-2005 -BLG-071Lb	0.46 ±0.04	Subsolar?[a]	3300 ±400	3.5[b] ±0.3	– –	3.6[b,c] ±0.2	This Paper

[a] While the metallicity of the OGLE-2005-BLG-017Lb host star is not directly constrained by our data, its kinematics indicate it is likely a member of the metal-poor thick disk.

[b] We give the planet mass and projected separation for the wide solution, which is favored by $\Delta\chi^2 \sim 4$. The second, close solution has $M_p = 3.3 \pm 0.3\ M_{\rm Jupiter}$ and $r_\perp = 2.1 \pm 0.1$ AU.

[c] We give the the projected separation between the host and planet at the time of event, which is the orbital parameter most directly constrained by our observations. However, assuming a circular orbit, we infer that the semi-major axis is likely only $\sim 30\%$ larger [a(wide) ~ 4.7AU, a(close) ~ 2.8AU].

References. — (1)Rivera et al. 2005; (2)Bean et al. 2006; (3)Benedict et al. 2002; (4)Butler et al. 2006; (5) Johnson et al. 2007b (6) Gaudi et al. 2008